A Dissertation

entitled

Evaluation of Large Area Polycrystalline CdTe Detector for Diagnostic X-ray Imaging

by

Xiance Jin

Submitted to the Graduate Faculty as partial fulfillment of the requirements for

The Doctor of Philosophy in Physics

(Area of Specialization: Radiation Oncology Medical Physics)

_____

E. Ishmael Parsai, Ph.D., Committee Chair

_____

Dianna Shvydka, Ph.D., Committee Member

_____

Michael Dennis, Ph.D., Committee Member

_____

Scott Lee, Ph.D., Committee Member

_____

Thomas Kvale, Ph.D., Committee Member

_____

Dr. Patricia R. Komuniecki, Dean
College of Graduate Studies

The University of Toledo

August 2011

An abstract of

Evaluation of Large Area Polycrystalline CdTe Detector for Diagnostic X-ray Imaging

by

Xiance Jin

Submitted to the Graduate Faculty as partial fulfillment of the requirements for

The Doctor of Philosophy in Physics

(Area of Specialization: Radiation Oncology Medical Physics)

The University of Toledo
August 2011

Introduction of digital radiography systems and successive use of flat panel detectors revolutionized the field of diagnostic imaging. Wide dynamic range, high image quality, real-time image acquisition and processing, precise image recording, and ease of remote access are among the most prominent improvements. One of the decisive factors contributing to further advancements remains the continuous development of different X-ray detecting materials, from traditional phosphor screens in combination with secondary photodetectors for indirect detection to use of thin-film photoconductors in direct detection systems. The latter approach offers a two-fold benefit: simpler device structure resulting in lower manufacturing cost, and a high potential of providing

images of superior contrast and sharpness due to inherently low signal spreading within the detector.

In the direct detection approach X-rays are absorbed by a photoconductor layer and converted to electron-hole pairs, which are then collected as electric charges on storage capacitors. Up to now amorphous selenium (a-Se) is the only photoconductor developed into direct detection type commercial medical imagers, for both general radiography and mammography applications. Detectors based on a-Se offer superior spatial resolution due to the simple conversion process. However, low atomic number and density (Z=34, ρ= 4.27 g/ cm^3), leading to low X-ray absorption, and high effective ionization energy (~50 eV) result in inadequate sensitivity, especially important for low exposure levels of fluoroscopic mode.

Materials of high atomic number and density have been investigated to replace a-Se. The purpose of this work is to evaluate polycrystalline Cadmium Telluride (CdTe) semiconductor material for application in large area diagnostic X-ray digital imaging in the direct detection configuration. Its high atomic number and density (Z=50, ρ= 5.86 g/cm^3), low effective ionization energy (~5eV), as well as wide band gap, makes CdTe very attractive for room temperature radiation detection applications. Recent developments in large area photovoltaic applications of CdTe have moved this photoconductor to the frontiers of thin-film manufacturing and large area medical imaging.

The intrinsic image quality characteristics of the polycrystalline CdTe detector under diagnostic X-ray imaging have been investigated by Monte Carlo simulation

using MCNP5 software package. The modulation transfer function (MTF), noise power spectrum (NPS), and detective quantum efficiency (DQE) of detectors of various thickness for diagnostic X-ray beams from 70 kVp to 120 kVp were determined. Thin film CdTe detector device operation was modeled with 1-D SCAPS (solar cell capacitance simulator) software package based on the energy deposition profiles obtained for diagnostic X-ray beams with Monte Carlo simulation. The sensitivity, linearity, and time response of prototype thin film CdTe detectors were measured. Electronic characteristics of a subset of thin detectors were verified against SCAPS simulation results allowing for model adjustments.

In this work we 1) calculate the diagnostic X-ray spectra of our Varian Ximatron simulator based on the measured output by tungsten anode spectral model using interpolation polynomials (TASMIP) technique，2) study image quality characteristics, such as MTF, NPS, and DQE with MCNP5 Monte Carlo simulations, 3) investigate the device operation with SCAPS simulations, and 4) measure the device performance with a set of prototype devices. Based on our simulation and measurement results, we believe thin film polycrystalline CdTe is a promising material for direct detection large area digital medical imaging.

Acknowledgements

I am deeply grateful for having Dr. E. Ishmael Parsai as my major advisor for my graduate studies during my stay at the University of Toledo. He has given me not only the guidance, support, and opportunities in my study and research, but also invaluable help and support on my life and my family. Without his help and support, I could not enjoy my graduate life here, and this Dissertation work will not be possible.

I would like to express my greatest appreciation to Dr. Dianna Shvydka for her insights and suggestions in MCNP Monte Carlo simulation and medical imaging. She has a remarkable ability to generate plausible explanations for seemingly incongruous results. I also thank the rest of my Dissertation committee members: Dr. Michael Dennis, Dr. Scott Lee, and Dr. Thomas Kvale for their review and valued input into my research.

I would like to take this opportunity to express my gratitude to the professional faculty and staff of the Radiation Oncology Department at the University of Toledo Medical Center for their contributions that allowed me to accomplish this work and their support for my preparation as a Medical Physicist, Dr. John J. Feldmeier, Dr. David Pearson, Nicholas Sperling, Dianne Adams, and many others.

Last but not least, special thanks to my beloved family: Meixiao Shen, my wife; Buyao Jin, my daughter; Dazuo Jin and Chunhua Wu, my parents; Renjun Shen and Qiushui Yu, my parents in-law, Taoju Jin and Taogui Jin, my sisters, and Lanxiao Shen, my sister in-law for their moral support, encouragements and help.

Table of Contents

List of Tables

List of Figures

List of Abbreviations

AMFPI	Active Matrix Flat Panel Imager
a-Se	Amorphous Selenium
a-Si:H	Hydrogenated Amorphous Silicon
CdS	Cadmium Sulfide
CdTe	Cadmium Telluride
CdZnTe	Cadmium Zinc Telluride
CSS	Close-Spaced Sublimation
DFT	Discrete Fourier Transform
DQE	Detective Quantum Efficiency
DSNR	Differential Signal-to-Noise Ratio
ECUT	Electron Cut-Off Energy
FFT	Fast Fourier Transform
FWHM	Full Width at Half Maximum
HgI_2	Mercuric Iodide
HPB	High-Pressure Bridgman
I-V	Current-Voltage
LSF	Line Spread Function
MC	Monte Carlo
MCNP	Monte Carlo N-Particle
MTF	Modulation Transfer Function

NIST	National Institute of Standard and Technology
NPS	Noise Power Spectrum
PbI_2	Lead Iodide
PhO	Lead Oxide
PV	Photovoltaic Device
PVD	Physical Vapor Deposition
SCAPS	Solar Cell Capacitance Simulator
SF	Scatter Fraction
SID	Source Image Distance
SNR	Signal-to-Noise Ratio
SnO_2	Tin Dioxide
SPR	Scatter-to-Primary Ratio
SRH	Shockley-Read-Hall
SSD	Source to Surface Distance
TASMIP	Tungsten Anode Spectral Model using Interpolation Polynomial
TFT	Thin Film Transistor
THM	Traveling Heater Method
TlBr	Thallium Bromide

Chapter 1

Introduction

Replacing analog X-ray imaging detectors (such as film-screen and X-ray imaging intensifier systems) with digital counterparts has long been of a primary interest to the medical community. The motivation for advancing towards the digital approach stems from a need to further improve image quality, reduce patient dose, increase patient throughput in the imaging center, and decrease overall costs. In recent years, this transition has been accelerated through the introduction of clinically practical devices based on large area active matrix flat-panel imagers (AMFPIs).[1,2,3]

1.1 Active matrix flat panel imagers (AMFPI)

A typical active matrix flat panel imager consists of the following components: a glass substrate, an X-ray converter, and external electronics.[4,5] The substrate is covered with a monolithically integrated circuit consisting of a two-dimensional array of imaging pixels.

The X-ray converter is directly built on the active matrix to create the imaging panel. There are two types of converter materials, photoconductor and phosphor. A photoconductor is generally referred to as a direct X-ray conversion material because X-rays are directly converted to electrical charges. A phosphor is known as an indirect

X-ray conversion material because X-rays are first converted to optical signal, then to electrical charge.[6] In the latter case each pixel includes a photodiode, e.g. hydrogenated amorphous silicon (a-Si:H), coupled to a storage capacitor. This is the so called active matrix, thin film transistor (TFT). It can read the incoming imaging signal and convert it to the output signal. The function of the external electronics is to control the operation of the array and transform the imaging information into digital form.

The numerous advantages of AMFPIs, including wide dynamic range, high image quality, real-time image acquisition and processing, precise image recording, and ease of remote access, have led to their widespread acceptance in an increasing number of medical applications, including radiography, fluoroscopy, cardiac imaging, mammography and radiotherapy imaging.[2,7,8,9,10,11,12,13] One of the decisive factors contributing to further advancements of AMFPI based digital imaging systems remain the continuous development of different X-ray detecting materials, from traditional phosphor screens in combination with secondary photodetectors for indirect detection to use of thin-film photoconductors in direct detection systems. The latter approach offers a two-fold benefit: simpler device structure resulting in lower manufacturing cost, and a high potential of providing images of superior contrast and sharpness due to inherently low signal spreading within the detector.

In the direct detection approach X-rays are absorbed by a photoconductor layer and converted to electron-hole pairs, which are then collected as electric charges on storage capacitors. Up to now amorphous selenium (a-Se) is the only photoconductor developed into direct detection type commercial medical imagers, and is found in both

general radiography and mammography applications.[14,15,16,17] Detectors based on a-Se offer superior spatial resolution due to the simple conversion process. However, low X-ray absorption and high effective ionization energy (~50 eV) result in inadequate sensitivity, especially important for the low exposure levels of fluoroscopic mode.[18]

To overcome this problem, materials of high atomic numbers and densities, such as mercuric iodide (HgI_2),[19,20,21] lead iodide (PbI_2),[22,23,24] lead oxide (PbO), [25] thallium bromide (TlBr), [26] and cadmium telluride/cadmium zinc telluride (CdTe/CdZTe)[27,28,29,30] have been suggested to replace a-Se. All of these materials possess an effective ionization energy about 10 times lower than that of a-Se, the substantially large band gaps necessary for minimization of leakage currents at room temperature, and a high mobility-lifetime product, providing effective charge collection.[25,31,32] Table 1-1 shows some of the major characteristics of these direct detection materials.

Due to the large area requirements imposed on practical medical imaging detectors, all of these materials are investigated in polycrystalline (thin-film) rather than single crystal form. This entails development of proper techniques for thin-film deposition in order for the material to be commercially viable. Since a-Se has been studied the longest, by now the capabilities to manufacture high quality films as thick as 1 mm have been proven. For other photoconductors this is still a subject of ongoing research, rendering use of some of the materials rather challenging. For example, strong temperature dependence on TlBr's conductivity makes it difficult to operate at room temperature;[26] poor response time and some limitations on film thickness are

detrimental to PbI_2 based device performance;[22] chemical stability, non-uniform sensitivity, and high levels of dark currents are still somewhat problematic in HgI_2 devices,[19,20] although the last material appears to be one the most promising.

Table 1-1 Main features of direct detection imaging materials.

	CdTe	$Cd_{0.9}Zn_{0.1}Te$	Se	HgI_2	PbI_2	TlBr	PbO_2
Atomic number	48,52	48,30,52	34	80,53	82,53	81,35	82,8
Density (g/cm^3)	6	5.78	4.3	6.4	5.0	7.56	9.58
Energy gap(eV)	1.44	1.57	1.7	2.13	2-2.5	2.68	1.9
Effective ionization energy(eV)	4.43	4.6	50	4.2	5-6	6.5	6

1.2 CdTe detectors

Due to its high atomic number, high density and wide band gap, CdTe ensures high detection efficiency, good room temperature performance, and is very attractive for room temperature radiation detection applications. Single crystal CdTe has been studied as an X-ray and gamma ray detector material since the 1960s.[33] Since then, quantitative studies have been carried out on the application of CdTe and its ternary alloy CdZnTe on X-ray imaging,[34] gamma ray imaging,[35] X-ray fluorescence analysis,[36] astrophysics research,[37] industrial gauging,[38] nuclear proliferation treaty verification,[39] and high energy industrial radiography and tomography.[40]

High purity CdTe crystals are usually grown by traveling heater method (THM)[41] and high-pressure Bridgman (HPB)[42] technique, doped with Cl to compensate for background impurities and defects. High work function metals, such as gold and

platinum, are used to form Ohmic contacts to fabricate CdTe detectors. One of critical issues of crystalline CdTe detectors is their time instability under bias, the so called polarization effect. Polarization is mainly caused by the trapping and de-trapping of the charge carriers that affect the space-charge distribution and the electric field profile in the detectors.[43] By applying high bias voltages and implementing low temperature operation, it is possible to minimize the polarization effect.[43] Low charge collection efficiency and non-ideal Ohmic contacts of CdTe detectors also limit their uses for medical imaging applications.

Recent developments in large area photovoltaic applications of CdTe have moved this photoconductor to the frontiers of thin-film manufacturing and large area medical imaging application. After several years of study, solar cells based on CdTe seem to be ripe for starting significant industrial production. A stable efficiency of 15.8% has been demonstrated for a 1 cm^2 laboratory cell[44] and it is expected that an efficiency of 12% can be obtained for 0.6×1.2 m^2 modules. Low cost soda-lime glass can be used as a substrate; the amount of source material is at least 100 times less than that used for single crystal modules and is a negligible part of the overall cost. Based on a bove mentioned reality, it is concluded that the technology to fabricate CdTe/CdS thin film solar cells is mature for large-scale production of CdTe based modules.[45] This makes polycrystalline thin film CdTe a very promising material for large area AMFPI application.[27,29] While the typical thickness of a solar cell is under 10 μm, the device deposition methodologies and post-deposition treatments for grain boundary passivation are essentially the same, and are successfully implemented in fabrication of

X-ray detectors up to 600 μm thick.[27,28]

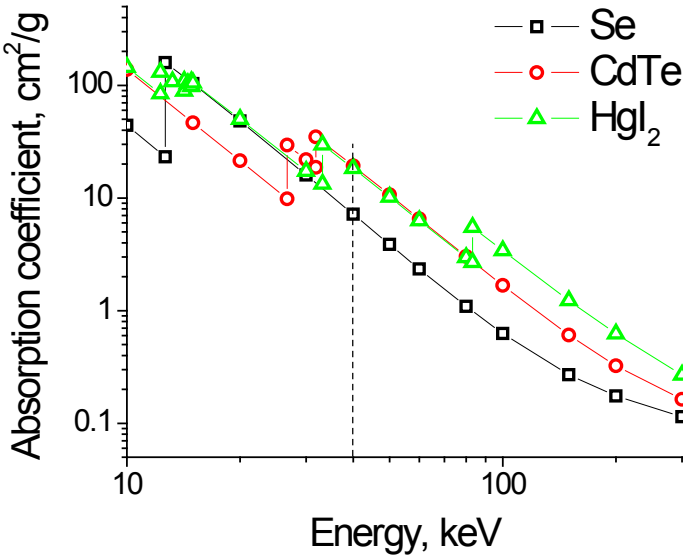

Fig. 1-1 Comparison of absorption coefficients for Se, CdTe, and HgI_2, Sharp jumps from left to right corresponding to the K-edges of Se (12.7 keV), Cd (26.7 keV), Te (31.8 keV), I (33.2 keV), and Hg (83 keV), respectively.

Even though the average atomic number of CdTe is lower than that of HgI_2, their absorption properties are very similar over a wide range of kV X-ray energies. Comparison of absorption coefficients [46] in Fig. 1-1 points out that for energies up to the K-edge of mercury (83 keV) both materials are equally superior to a-Se. Coincidently, even for the spectra corresponding to higher kV potentials (up to 140 kVp) most of X-rays have energies this range. Proven outstanding radiation hardness of CdTe[47,48,49,50,51] makes it an ideal candidate for large area imaging applications.

The development of new detectors for medical imaging is a complex and expensive endeavor. An understanding of fundamental performance potential and limitations of a

new imaging system is therefore critical to the wise allocation of research resources. The performance of polycrystalline CdTe detector under an 80 kVp diagnostic X-ray beam has been studied by one Japanese group with a 200 μm thick prototype, and showed a sensitivity of 10 times higher than that of a-Se.[28,29] The spatial resolution of the CdTe under monoenergetic diagnostic X-ray beams has also been conducted. [52] However, up until now no systematic study on the performance of thin film polycrystalline CdTe detector for diagnostic X-rays has been performed. In this Dissertation, the performance of thin-film CdTe of thickness, from 2 μm up to 1000 μm, under a range of spectra relevant to diagnostic imaging application, from 70 kVp to 140 kVp, was studied.

Chapter 2

Diagnostic X-ray Spectra Calculation

Computer simulation of X-ray spectra is one of the most important tools for radiation detector investigation, owing to the experimental complexity of measuring X-ray spectra. There are several types of methods for X-ray spectra prediction, mainly empirical models,[53] semi-empirical models,[54] and Monte Carlo modeling.[55] Each model has its advantage and disadvantages.[54] An empirical model, tungsten anode spectral model using interpolating polynomials (TASMIP) technique,[53]was applied in this study.

2.1 Tungsten anode spectral model using interpolating polynomials (TASMIP)

The TASMIP is an empirical algorithm and uses no physical assumptions regarding X-ray production, but rather interpolates measured constant potential X-ray spectra published by F ewell et al.[56] It has been shown to be able to accurately reproduce both the kV-dependent spectral shape and output fluence for X-ray machines employing a tungsten target.[53]

The X-ray output of the Varian simulator (Ximatron, Varian, Palo Alto, CA) in our department was measured in the units of mR/mAs at a distance of 1000 mm from the focal spot using an Unfors Xi External Detector. Output measurements over the kVp of 40, 50, 56, 60, 66, 70, 76, 80, 86, 90, 96, 100, 106, 110, 116, 120, 125 were measured

at the settings of 200 mA, 50 ms (10 mAs) with 0, 1.0, 2.0, 3.0, 4.0, and 5.0 mm added aluminum filtration. The exposure readings were divided by 10 mAs to convert units of milli-Roentgen to mR/mAs at 1 m. At each of the six aluminum thicknesses, the mR/mAs values were fit as a function of kV to a four-term (third order) polynomial expression using Matlab software. The polynomial fit results, expressing output as a function of kV for each thickness of aluminum, are reported in Table 2-1. The measured output results and their fit results are shown in Fig 2-1. The marked points show the actual measured values. The lines are the corresponding output of each set of measured points, fitted by t he four-term (third order) polynomial fit with Matlab software. The attenuation curves were calculated based on this fitted output.

Table 2-1 The polynomial fit coefficients of the X-ray tube output (mR/mAs @ 1 m) as a function of kV.

AL mm	a0	a1	a2	a3	a4
0.0	-79.57942844363720	4.11234821539501000	-0.06950044676700500	0.0007018716069716780	-2.27799710098037E-06
1.0	-19.32215619578240	0.69566253007426700	-0.00469296830128470	0.0001254102567911750	-4.30207996456507E-07
2.0	-24.99529448150460	1.12887468896744000	-0.01786274759154280	0.0002397230863917810	-7.86241147107836E-07
3.0	-3.41193493378052	-0.00267622764470925	0.00214219401958990	0.0000673958766349571	-2.55198459003597E-07
4.0	-10.00740205379560	0.39447895036691900	-0.00721207591368222	0.0001416396317492320	-4.78626295944874E-07
5.0	-6.86929250199113	0.26086186762276500	-0.00577575686078123	0.0001284495437752800	-4.45693745580963E-07

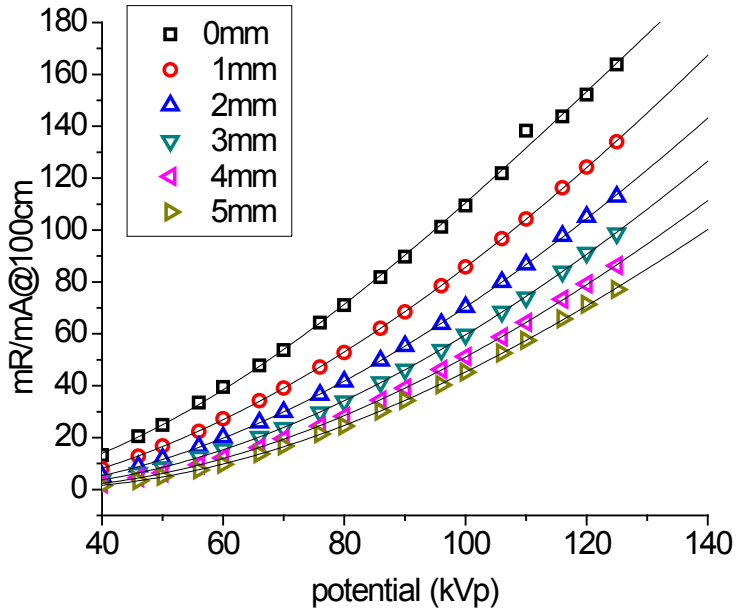

Fig. 2-1 The output of simulator with different thickness of aluminum filter, marked points show the measured data points, and the corresponding lines represent the polynomial fit to the data.

Unfiltered tungsten spectra from Fewell et al.[56] were tabulated for 70, 80, 90, 100, 120, 130, a nd 140 kV p and were linearly interpolated to 1 k eV intervals. These tabulated data correspond to the spectra labeled EI1 though EI8 on pages 43-45 of Ref 56. The attenuation curves of these unfiltered Fewell spectra were calculated based on the attenuation coefficients of aluminum from Physics Laboratory of National Institute of Standard and Technology (NIST).[46] To compensate for probable differences in the X-ray tube housing attenuation values at each kVp, additional thicknesses of aluminum were needed to be added to the inherent filtration of the Fewell spectra. A least square approach was used to minimize the difference in (percent) attenuation values between the simulator X-ray and the Fewell spectra. As shown in Fig. 2-2, the marked points are attenuation values calculated from the modified Fewell spectra, and the corresponding solid lines represent attenuation profiles calculated from simulator

output data. Additional aluminum thickness needed to match the Fewell spectra to the attenuation levels of simulator X-ray are given in Table 2-2.

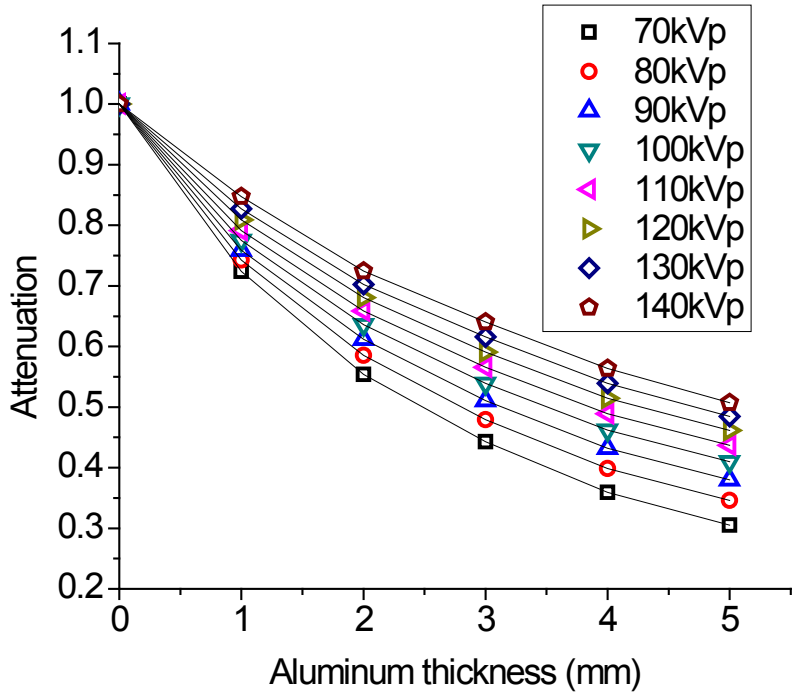

Fig. 2-2 Matched attenuation curves of simulator X-ray and Fewell spectra for different kVp based on the least square approach. The marked points are attenuation values calculated from the modified Fewell spectra, and the corresponding solid lines represent attenuation profiles calculated from simulator output data.

Table 2-2 Additional aluminum thicknesses needed to match the Fewell spectra to the attenuation levels of the simulator X-ray.

Potential (kVp)	70	80	90	100	110	120	130	140
Added aluminum thicknesses (μm)	557	700	802	1037	854	818	727	587

Once the Fewell spectral shapes were slightly hardened to best fit the simulator's attenuation values, the number of X-ray photons for each spectrum was normalized to the corresponding output of the simulator with no added filtration. We can, based on these modified Fewell spectra with additional aluminum thicknesses, calculate the

polynomial interpolating coefficients using the following equation:

$$\Phi[E] = a_0[E] + a_1[E]kVp + a_2[E]kVp^2 + a_3[E]kVp^3 \qquad (2\text{-}1)$$

Resulting coefficients are shown in Appendix A. With these coefficients, simulator X-ray spectra at any arbitrary kVp value can be computed. According to the real clinical situation, and the accuracy of the computation, we generated simulator spectra of 70, 80, 90, 100, 110, 120, 130, and 140 kVp as shown in Fig. 2-3 for the following Monte Carlo simulation. The sharp jumps are corresponding to the K_α and K_β of tungsten, respectively. The average percentage error between the modified spectra and the final interpolated spectra is around 0.1% to 1.9%.

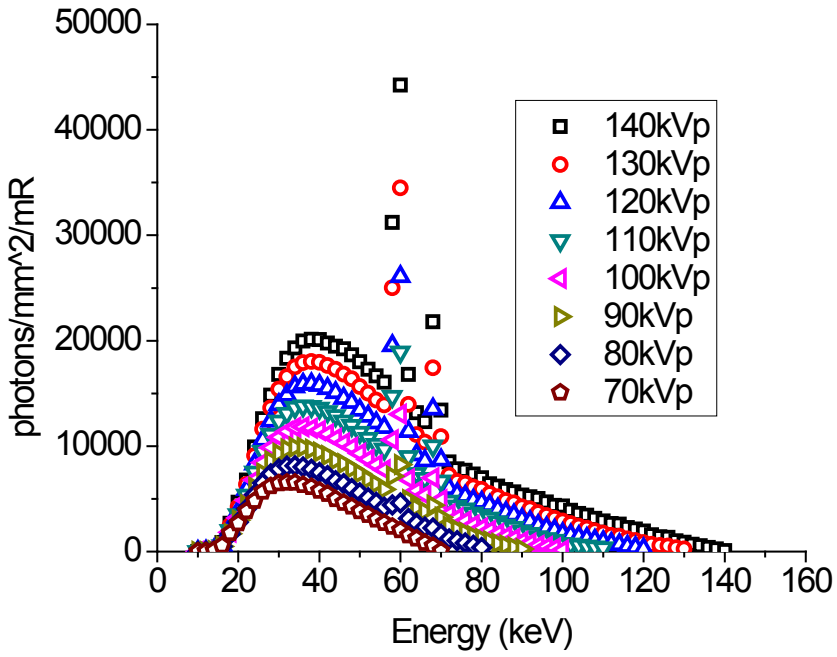

Fig. 2-3 Simulator spectra from 70 kVp to 140 kVp computed by polynomial interpolation on modified Fewell spectra

2.2 Exit spectra simulation

In practice, a patient is placed between the source and the detector. This has the effect of both hardening the primary spectrum and producing scattered photons and electrons. To properly model the response of the detector to the primary beam, we require the energy spectrum of the primary photons transmitted through the patient. We approximated the hardening of the spectrum from the simulator by assuming the patient to be equivalent to a 20 cm water phantom.

Monte Carlo (MC) radiation transport simulation package MCNP5 (Monte Carlo N-particle)[57] codes were written to calculate the primary exit spectra with the geometry shown in Fig. 2-4. The original spectra calculated in section 2.1 with a source distance 100 cm above the phantom were perpendicularly incident to a 20 cm water phantom slab. The exit spectra were tallied with an F1 tally at the surface of thin-film CdTe detector, which is 20 cm under the water phantom according to the clinical application with a source image distance (SID) of 140 cm. The tally cards are commands used in MCNP5 to specify what you want to learn from the Monte Carlo calculation. The function of F1 tally is to calculate the surface current. Using FT INC option for tally F1, we can tally the primary, scatter, and total beams separately, based on number of interactions. Fig. 2-5 (a) and (b) are the primary spectra before the water phantom and after traveling through the water phantom for energy of 80 kVp and 140 kVp, respectively. The sharp jumps are corresponding to the K_α and K_β of tungsten, respectively. It indicates that the scatter component is not negligible and is unavoidable in a realistic patient imaging procedure. These scatter beams after the water phantom

will reach the detector and introduce additional noise to the image. However, after the 20 cm air gap, the scatter photons that reached the detector were greatly reduced, as indicated by our simulation study on a 20×20 cm^2 field.

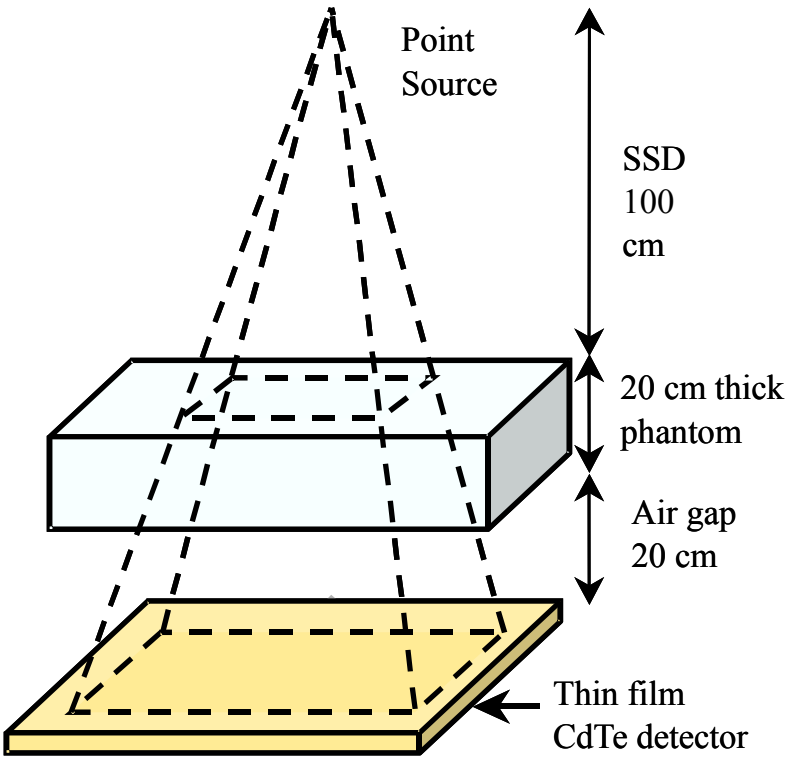

Fig. 2-4 Schematic illustration of the geometry setup used in Monte Carlo simulations of energy deposition and line spread function.

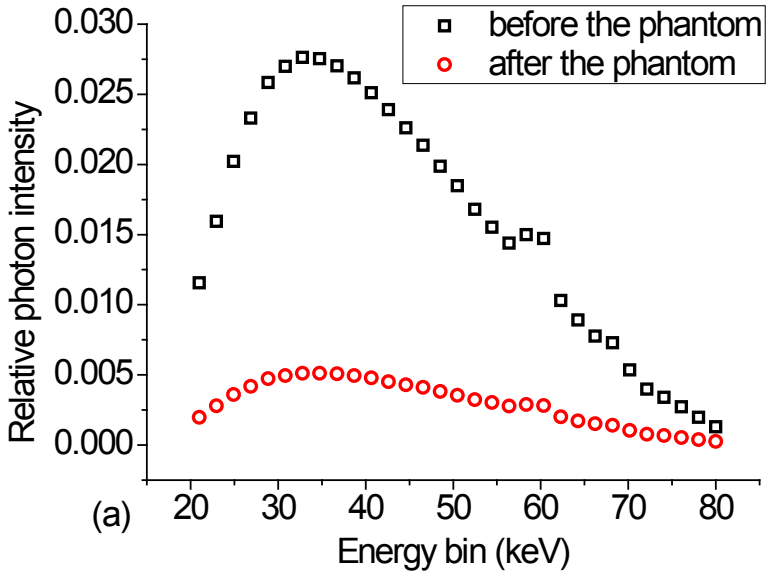

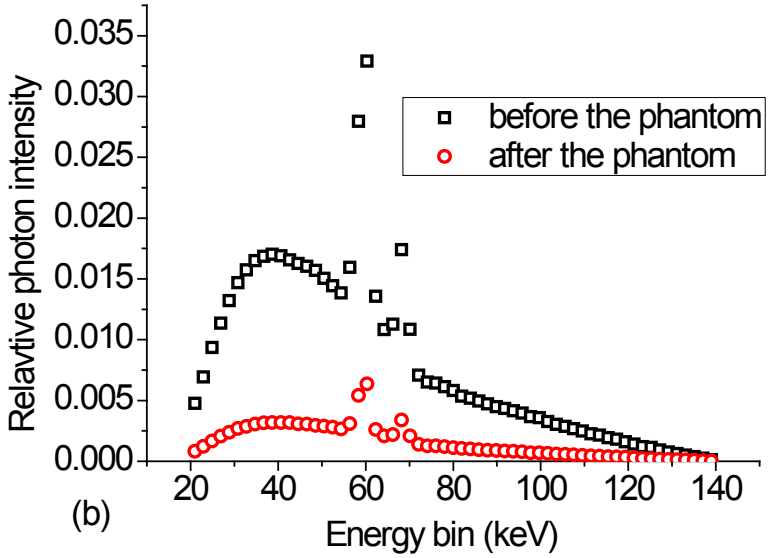

Fig. 2-5 Primary diagnostic spectra before the water phantom and after the water phantom (a) for 80 kVp; (b) for 140 kVp.

2.3 Influence of scattered particles

We simulated the scatter fraction (SF) and scatter-to-primary ratio (SPR) right at the surface of detector after the spectra pass through a 20 cm water phantom. Similar simulation geometry of Fig. 2-4 with a field size of 20 ×20 cm^2 was applied with the MCNP5 package. The photon source was put at 100 cm SSD above the 20 cm water phantom. Primary and scatter beams were tallied by using FT INC option of tally F1 separately.

Photons scattered by the patient and the secondary electrons produced in the patient will degrade both image contrast, C, and differential signal-to-noise ratio, DSNR.[58] The loss of contrast due to energy deposition is given by

$$\frac{C_s}{C_{ns}} = 1 - SF \qquad (2\text{-}2)$$

Where C_s and C_{ns} are the image contrast with and without the presence of scattering, respectively. SF is the scatter fraction, given by

$$SF = \frac{E_s}{E_p + E_s} \qquad (2\text{-}3)$$

where E_p and E_s are the average energy deposited by the primary and scattered beams, respectively. The loss in DSNR is given by

$$\frac{DSNR_s}{DSNR_{ns}} = \frac{1}{\sqrt{1+SPR}} \qquad (2\text{-}4)$$

where $DSNR_s$ and $DSNR_{ns}$ are the DSNR with and without the presence of scatter, and SPR is the scatter-to-primary ratio, which is defined by

$$SPR = \frac{\sigma_{E_S}^2}{\sigma_{E_p}^2} \qquad (2\text{-}5)$$

where σ_{E_p} and σ_{E_s} are the standard deviation in the quantities E_p and E_s, respectively,

$$E_{p,s} = \frac{1}{N}\sum_{i-1}^{N} E_{i_{p,s}} \qquad (2\text{-}6)$$

and $$\sigma_{E_{p,s}} = \sqrt{\frac{1}{N}\sum_{i-1}^{N} E_{i_{p,s}}} \qquad (2\text{-}7)$$

As we can see from Fig. 2-6, both SF and SPF are relatively small and show a trend of increasing with energy. More clearly from Fig. 2-7 we can see both of the contrast and the DSNR are very close to unity, although the contrast and differential signal-to-noise ratio (DSNR) decrease with the potential energy.

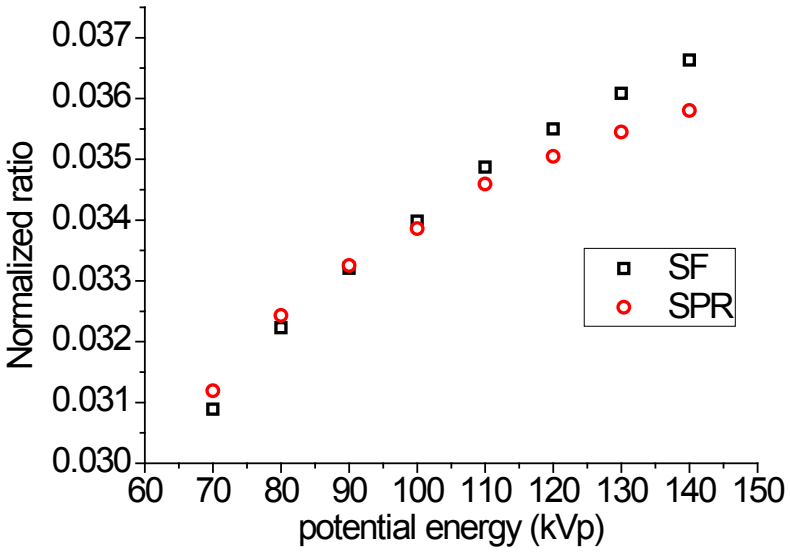

Fig. 2-6 Scatter fraction and scatter-primary ratio at the surface of detector after spectra traveling though a 20 cm water phantom.

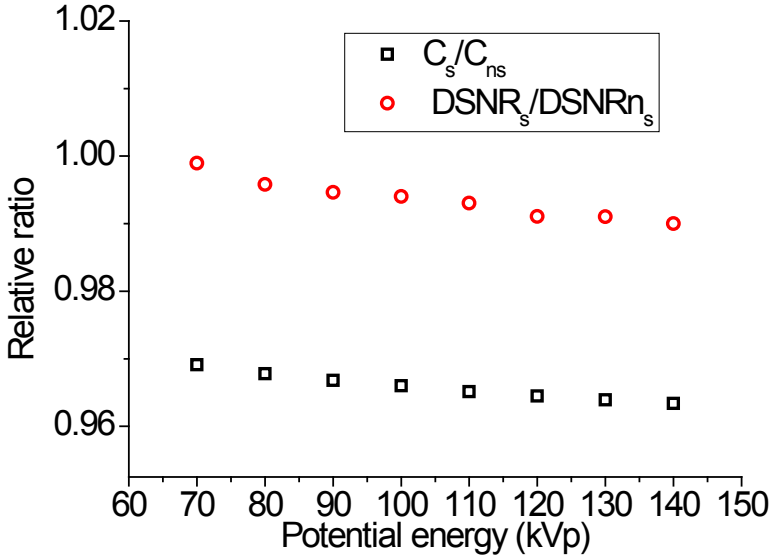

Fig. 2-7 Contrast and differential signal-to-noise loss caused by the scattered particles after the X-ray spectra traveling through a 20 cm water phantom.

Only primary photon beams were used to evaluate the performance characteristics of the detector. In all Monte Carlo simulations we used CdTe thin-film density ρ=5.86 g/cm^3. The electron cut-off energy (ECUT) was chosen so that the electron range at

ECUT is less than 1/3 of the smallest dimension in the dose scoring region, 0.02 MeV for 20 micron scoring slit.[59,60] The cut-off energy for photons was set to 0.01 MeV, with coherent, photonuclear and Doppler interactions turned off.

Chapter 3

Modulation Transfer Function

3.1 Interactions and spatial resolution

Direct detection design imagers, utilizing photoconductor materials usually possess a higher spatial resolution than their indirect detection counterparts employing phosphors or scintillators in combination with a photodiode. In the former, the X-rays were directly converted into electrical charges in the photoconductor. By contrast, in the latter design X-rays are first converted into optical photons in phosphor or scintillator, then into electrical charges in a photodiode. The intermediate stage involving optical photon conversion introduces an additional lateral spreading in the imaging process, thus decreasing the modulation transfer function of the imaging system.

In the diagnostic X-ray energy range, the relevant X-ray interaction processes are photoelectric absorption, coherent interaction (Rayleigh scattering) and incoherent interaction (Compton scattering). The relative probability of occurrence for each interaction is shown in Fig. 3-1 as a function of X-ray energy for CdTe.[46] As can be seen from the graph, photoelectric absorption is dominant over the entire diagnostic energy range.

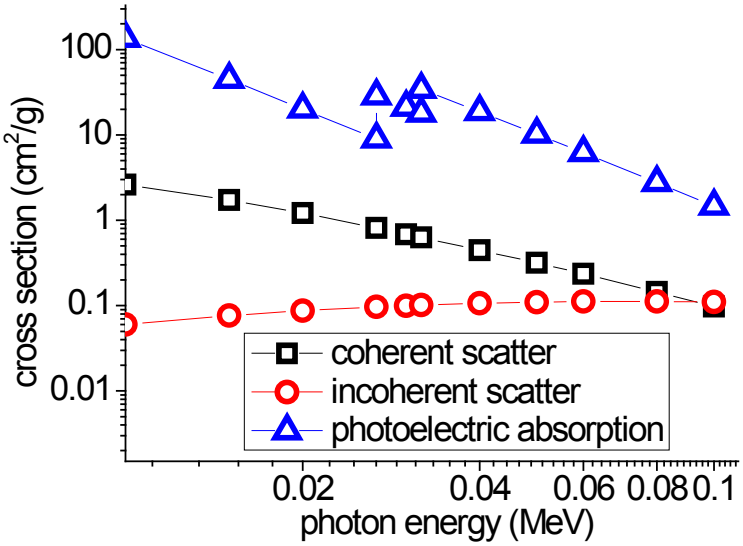

Fig. 3-1 Photoelectric absorption, coherent and incoherent cross section of CdTe under diagnostic X-ray beams.

In the photoelectric effect, the energy of the incoming X-ray is fully absorbed by the material atom. Electrons are emitted from the atom shell as the consequence of this energy absorption.[61,62] The resultant atom is left in an excited state, and returns to the ground state through a cascade of electron transitions, resulting in the isotropic emission of characteristic X-rays and Auger electrons. Rayleigh scattering can cause the atom to emit an X-ray that leaves the atom at an angle relative to the incident X-ray, although there is no energy absorption during the process. Compton scattering will cause the incoming X-ray to be scattered with a reduced energy, and cause the atomic electron to recoil in a direction within the same plane as the scattered X-ray.

Depending on the energy of incoming X-ray and the physical properties of the detector material, the spatial resolution of the detector can be significantly degraded by the secondary radiation, such as scattered photons and electrons generated.[63] The loss of spatial resolution is caused by the "blurring" or "spreading" of the incident energy.

Not all of the energy is deposited at the primary interaction site. Secondary particles move part of the incoming energy away from the primary interaction site. The degree of spreading depends not only on the energy of the secondary radiation, but also on the direction that the radiation is emitted from the primary interaction site. The scattering angle of the secondary particles is generally a complex function of radiation energy and detector composition (e.g. atomic number). Therefore, Monte Carlo methods are usually utilized in order to properly simulate and isolate the effects of the X-ray interaction processes on spatial resolution.[52,63,64]

Monte Carlo simulation of the intrinsic spatial resolution of CdTe for monoenergetic X-ray beams has been previously performed, indicating severe degradation of spatial resolution with energies right above the K-edges of Cd and Te, which are 26.7 ke V and 32.8 ke V, respectively.[52] However, in clinical conditions, medical imaging is performed with a broad X-ray spectra, instead of monoenergetic beams. In this chapter, the diagnostic X-ray spectra described in Chapter 2 were applied to simulate the spatial resolution characteristic of CdTe for diagnostic X-ray beams.

3.2 Monte Carlo simulation method

Spatial resolution is usually characterized quantitatively through the modulation transfer function (MTF). The MTF offers a complete description of the resolution property of an imaging system. It illustrates the fraction (or percentage) of an object's

contrast that is recorded by the imaging system, as a function of the size (i.e., spatial frequency) of the object. MTF can be obtained by a Fourier transform of the line spread function (LSF) as:

$$MTF(f) = \int_{-\infty}^{\infty} LSF(x) e^{-i2\pi fx} dx \qquad (3\text{-}1)$$

MC codes for a geometry similar to that in Fig. 2-4 (second part, after the water phantom) were written to simulate the energy deposition in the thin-film CdTe detector of different thickness, 100, 300, 600, and 1000 μm. The detector was placed at a distance of 140 cm from the source. The primary X-ray beam, after going through the water phantom with X-ray tube voltages of 70 to 140 kVp, was set to fall normally on the detector surface through a narrow slit, following a typical setup for line spread function LSF(x) measurement,[65] as shown in Fig. 3-2. To characterize the LSF(f) , the detector was divided into 512 strips on each side of the slit source with a width of 10 μm, and a length of 30 cm , which according to the Nyquist criterion gave a cutoff frequency of 50 mm^{-1}. A total number of 1024 points were selected to simulate a smooth LSF(x) curve. Increasing the number of points by 2 did not affect the shape of the resulting MTF(f). A photon line source with a width of 2 μm was incident perpendicular to the detector and the energy deposition was collected with a *F8 tally, which is a command to calculate the energy distribution in MeV. Following the general rule of thumb for calculating dose distributions, the electron cut-off energy (ECUT) was chosen so that the electron range at ECUT is less than 1/3 of the smallest dimension in the dose scoring region.[59,60] So cut off energies of 0.02 Mev for electrons and 0.01 MeV for photons were selected, with coherent, photonuclear and Doppler

interactions turned off. A history of 10 million photons was run. The MTF(f) was calculated with Eq. (3-1) by performing a fast Fourier transform (FFT) to the LSF(x) with Hanning window.

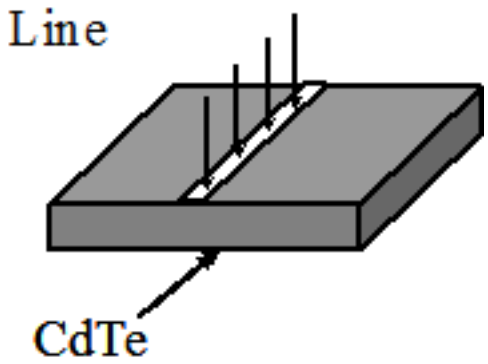

Fig. 3-2 Narrow slit Monte Carlo simulation geometry for line spread function.

3.3 Simulation results

Line spread function defines the absorbed energy distribution in a narrow slit. Fig. 3-3 is a typical line spread function of 600 μm we calculated on a linear scale from Monte Carlo simulation. As we can see, the detector has a sharp response to the diagnostic X-ray beam.

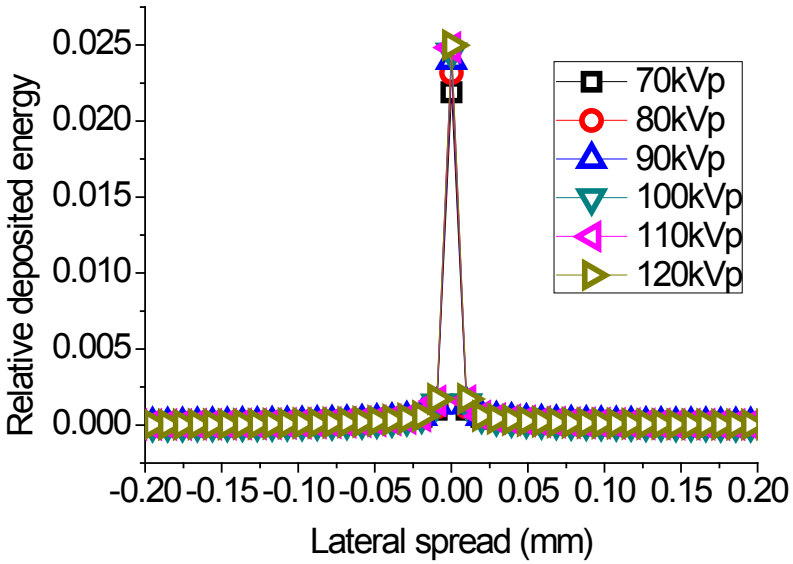

Fig. 3-3 LSF of 600 μm CdTe for different energy.

Fig. 3-4 (a) illustrates the MTF of thin film CdTe with thicknesses from 100 μm to 1000 μm for an 80 kVp beam. As expected, the MTF of CdTe decreases with the thickness, but the decrease becomes moderate after 300 μm. From Fig. 3-4 (a), at spatial frequency of 5 mm^{-1}, the MTF of 300 μm decreases about 6.1% compared to that of 100 μm, while the MTF of 600 μm only decreases 1.4% compared to that of 300 μm. The decrease is Even less for 1000 μm, which decreases only 0.2% compared to that of 600 μm. The MTF decreases with increasing of detector thickness results from the increase in the amount of photon scatter, and due to the increase in re-absorption fraction of K-fluorescent X-ray with the thickness of detector. Fig. 3-4 (b) shows the MTF of 600 μm thick CdTe under multiple energies from 70 kVp to 120 kVp. For the frequency range of about 3 to 15 mm^{-1}, the lowest energy beam produces lowest MTF. This is due to the lower energy spectrum having a larger portion of incoming photons with energies just above the K-edges of both Cd (26.7 keV) and Te

(31.8 keV). The higher absorption results in production of a larger number of fluorescence photons, which can be re-absorbed up to 150 μm away from the origin. At higher frequencies (see Fig. 3-4 (b), insert), the MTF is more degraded at the higher beam energies due to the increase in probability of Compton interactions, resulting in scattered particles depositing their energy close to the first interaction site. The effective path lengths of recoil electrons increase with the increasing energy, resulting in increased lateral spread within the detector. This is consistent with the findings of previous studies.[66,67]

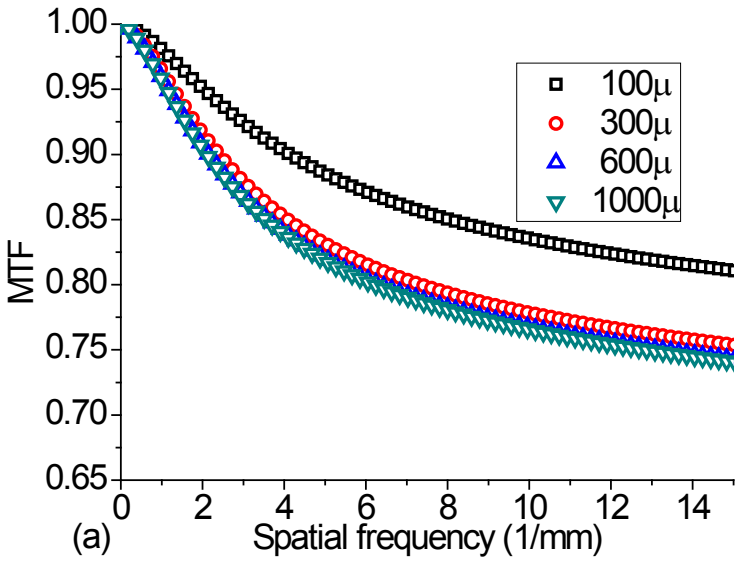

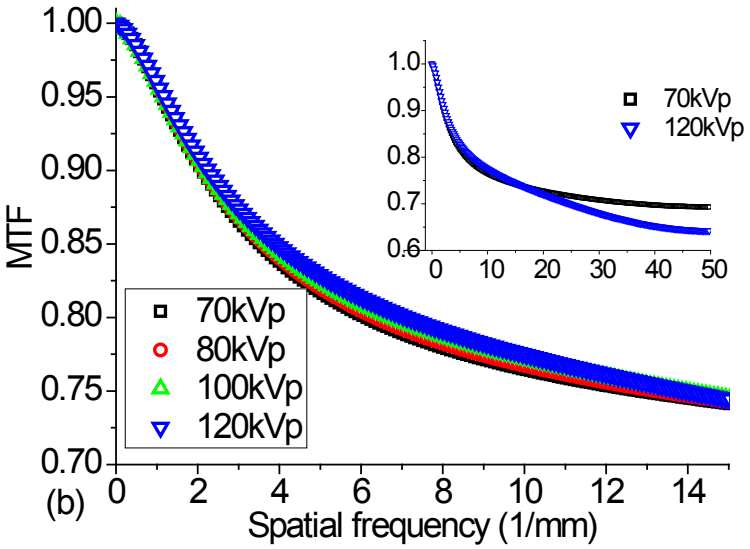

Fig. 3-4 (a) MTF of CdTe with thicknesses of 100, 300, 600, and 1000 μm for 80 kVp beam; (b) MTF of 600 μm CdTe for energies from 70 kVp to 120 kVp.

For the purpose of comparison, MTF of a-Se and Mercuric Iodide (HgI_2) of the same thickness were also simulated and compared with that of CdTe. As shown in Fig. 3-5, the MTF of a-Se and HgI_2 of the same thickness are a little better than that of CdTe. This is because the mean energy of an 80 kVp diagnostic X-ray spectrum is about 37 keV, which is right above the K-edges of Cd and Te, which is 26.7 keV and 31.8 keV. The K-edge of Selenium is only 12.7 keV. The MTF curve for energies directly above the K-edge energy drops steeply, while with increasing energy the MTF rise again. Right above the K-edge, the generated K-fluorescence will travel some distance from the initial interaction site. This effect spreads the signal in space, thus reducing the MTF in the lower spatial frequencies.

The K-edge of Hg is 83.1 keV, and for Iodine is 33.2 keV. So for the 80 kVp spectrum, CdTe shows a lower MTF due to a stronger re-absorption with characteristic

X-ray beams, as shown in Fig. 3-5 (a). This result agrees well with other Monte Carlo simulation results with monoenergetic X-ray beams.[32] At 120 kVp, this is no longer the case: where more photons with energies above K-edges of HgI_2 are present in the incoming beam, the MTF of CdTe is higher than mercuric iodide's, as evident from Fig. 3-5 (b). This is also because for the 120 kVp spectrum, where the Compton effect becomes more important, MTF was decreased in the high frequency range. The energy of scattered Compton quanta is much lower than that of the incident quanta. Therefore, they become absorbed in the vicinity of the first interaction.

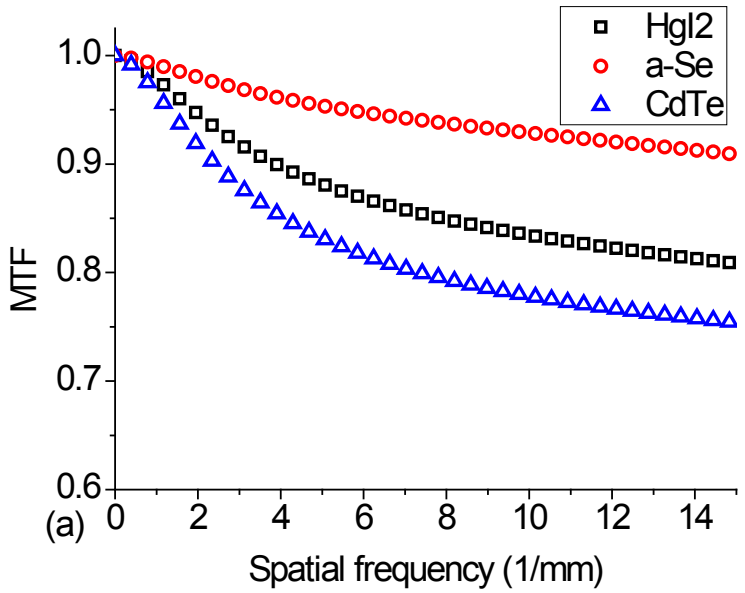

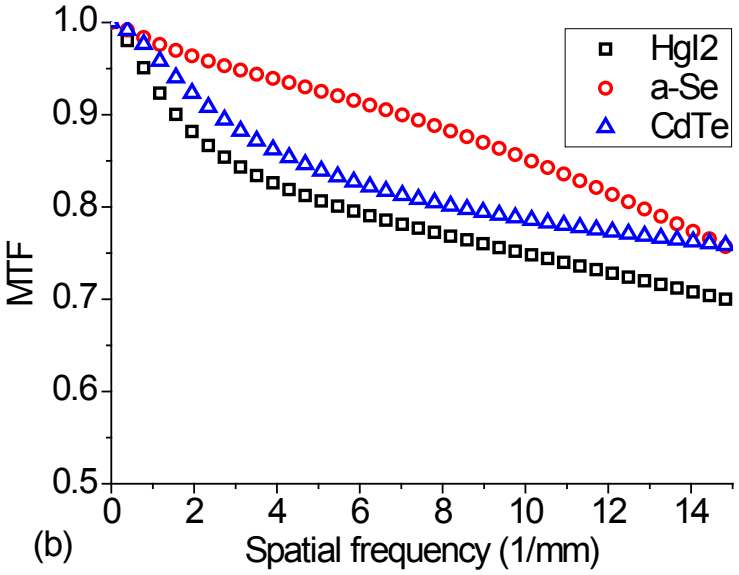

Fig. 3-5 MTF of three photoconductors with thickness of 300 μm (a) for 80 kVp beam; (b) for 120 kVp beam.

Chapter 4

Noise Power Spectra (NPS) Simulation

Because of its quantum nature, the transfer of information from the object to the image is inherently noisy. Noise is often defined as the uncertainty in a signal due to random fluctuations in that signal. There are many causes for these fluctuations. For example, an X-ray beam emerging from an X-ray tube inherently is stochastic in nature, that is, the number of photons emitted form the source per unit time varies according to a Poisson distribution. Other sources of random fluctuation are introduced by t he process of attenuation in materials present in the path of the radiation beam (patient, patient table, detector enclosure). Finally, the detectors themselves often introduce noise. Noise is therefore inherent in the radiographic imaging process and is caused by a number of different processes.

4.1 NPS simulation

Image noise is fundamentally limited by the statistical nature of image quanta,[68,69,70,71,72] and was subsequently described in terms of the noise equivalent number of quanta.[73,74] Among the various descriptors used to quantify imaging noise, the Wiener spectrum is the most complete characterization method. The Wiener spectrum does not only account for the magnitude of the noise, but also describes the "texture" through its frequency dependence.[75]

The noise transfer properties of the detector were studied by simulating the energy absorbed with MCNP5. The simulation geometry was similar to that used to obtain the MTF. A 30×40 cm^2 photon beam was perpendicularly incident on the X-Y plane of the detector. The detector plane was divided into multi-slit with M×N points. Energy deposition on each point of the multi-slit was simulated and recorded as one signal. Signal average and difference were calculated. The mean square departure of the signal from its average value is the variance and the analysis of this variance into frequency components gives the noise power spectrum.[76] Although a two-dimensional analysis of the NPS is necessary, sometimes, visualization in two dimensions can be problematic.[77] In many situations it is adequate to examine the two dimensional NPS in only one specified direction at a time.

One-dimensional (1-D) NPS was analyzed by a synthesized slit technique.[78] The energy absorption in the non-overlapping slits, each of dimensions 1*512 points, were tallied by *F8 and summed along the y direction. The slit dimension was 0.002×3 cm^2, providing a Nyquist frequency of 25 mm^{-1} in the x direction. A total of 10 million histories were run in order to get sufficient statistical deviation. The absorbed energy distribution slits were Fourier transformed using a 1-D FFT to yield power spectra. A total of 420 slits were averaged to yield the simulated NPS:

$$NPS(f) = \frac{x_0 y_0}{N_x N_y} \left\langle \left| DFT\left(\sum_{n_y=0}^{N_y-1} \Delta d_{n_x,n_y} \right) \right|^2 \right\rangle MeV^2 mm^2 \qquad (4\text{-}1)$$

Where x_0 and y_0 are the x and y spacing of the discrete values respectively. N_x and N_y are the number of elements (scoring voxels) in x and y dimensions, respectively.

DTF stands for Discrete Fourier transform. d_{n_x,n_y} is the energy deposited (in MeV) within the (x,y)-th element, and $\Delta d_{n_x,n_y} = d_{n_x,n_y} - < d_{n_x,n_y} >$, is the energy difference of each element to the mean absorbed energy.

4.2 NPS results and discussion

Quantum noise is due to statistical fluctuations in the number of X-rays interacting with the detector and statistical fluctuations in the number of electrons produced by the detector. As shown in Fig. 4-1 (a), the noise power spectrum increases with the thickness of detector. It is expected that more energy is absorbed and more electron hole pairs are generated as the detector thickness increases. Fig. 4-1 (b) shows that the noise power increases with increasing energy. With the increase of energy, more photons interact with detector and more electron hole pairs are generated. The fluctuation also increases according to Poison statistics.

It also shows a slight decrease trend with increasing frequency in Fig. 4-1. This indicates there is slight correlation between the absorbed energies. We applied a Lorentz nonlinear curve fitting function on these NPS as shown in the Fig. 4-1 the solid lines. The Lorentz nonlinear curve fitting function is:

$$y = y_0 + \frac{2A}{\pi}\frac{w}{4(x - x_c)^2 + w^2} \qquad (4\text{-}2)$$

Where w is the full width at half maximum, and y_0 and A are fitting parameters. The correlation length in mm, reflecting the smallest feasible pixel size for the detector, was estimated as w^{-1}. Typical values obtained for 300 to 1000 μm thick CdTe were in the

range of 0.1 mm, which is approximately the typical pixel size employed in digital imagers. [18]

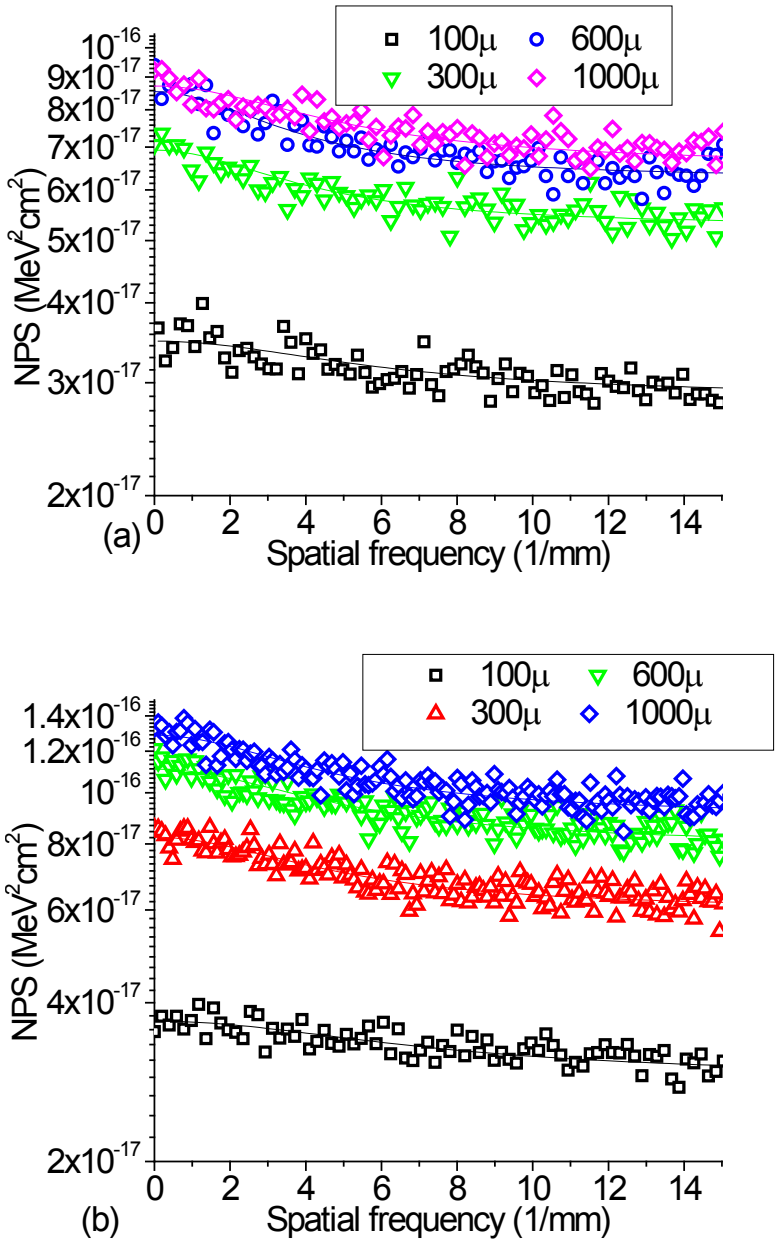

Fig. 4-1 Noise power spectra for (a) 80 kVp beam and (b) 120 kVp beam.

Fig.4-2 indicates that the statistical fluctuation of absorbed X-rays is the main source of quantum noise.[79] HgI_2 has the highest attenuation coefficient among these

three materials, as it interacts with more photons and more secondary quanta are generated than via a-Se and CdTe. According to Poisson statistics, HgI_2 has a most noise, and Se has the least noise among these three materials.

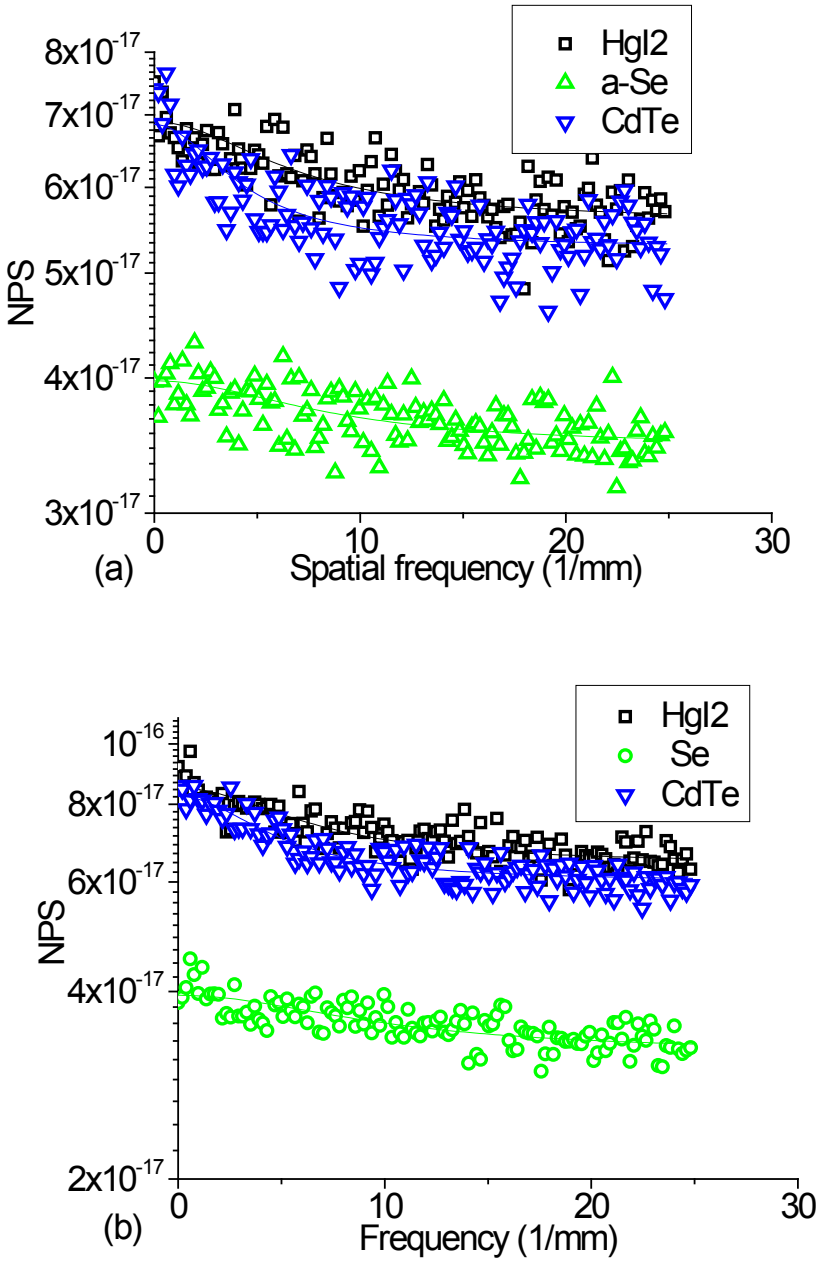

Fig. 4-2 NPS comparison among 300 μm thickness HgI_2, Se, and CdTe for (a) 80 kVp spectrum; (b) 120 kVp spectrum.

Chapter 5

Detective Quantum Efficiency

Image quality expressed in terms of the X-ray image signal-to-noise ratio (SNR) is a balance between imaging system performance and radiation risk to the patient, and it is critical to obtain the best possible SNR for a specified risk to the patient in order to satisfy the "as low as reasonably achievable" principle. One close related quantity to SNR is the detective quantum efficiency (DQE), which is defined as the squared ratio of the signal-to-noise (SNR) at the detector output to that at the detector input as a function of spatial frequency.[80]

5.1 DQE calculation

The detective quantum efficiency (DQE) has become the best single descriptor of radiographic detector performance. It gives a measure of how efficiently the imaging system makes use of the information content of a radiation beam. For an ideal imaging system, the DQE is equal to 1, but in reality it is degraded by different sources of noise associated with the system.

The DQE at zero frequency, DQE(0) is related to energy absorption properties only; it is the maximum DQE of the detector that can be achieved. When taking X-ray quantum detection noise into account, the DQE(f) can be expressed as: [81,82]

$$DQE(f) = \frac{A_0^2 MTF^2(f)}{\overline{q_0} NPS(f)} \qquad (5\text{-}1)$$

where A_0 is the mean signal value at the detector output and $\overline{q_0}$ is the incident X-ray fluence. In our MC simulations, pulse height tally *F8 was used to record the energy deposition within each detector element, averaged into the mean signal value A_0. Based on simulated MTF and NPS we found frequency-dependent detective quantum efficiencies for a set of kVp values for CdTe detectors of varying thicknesses. We note that DQE(f) obtained for each CdTe film thickness is a pre-sampling or intrinsic characteristic of the detector.

5.2 DQE results

Shown in Fig. 5-1 results for DQE(f) of 100 to 1000 μm thick CdTe were calculated using Eq. 5-1, based on MTF and NPS curves calculated in previous chapters, where NPS dependences were fitted with Lorentz functions. DQE(f) improves with increasing thin film CdTe thickness due to an increase in the number of absorbed photons. However, a thicker detector also provides longer paths for the lateral spread of secondary electrons and photons, resulting in a loss of spatial resolution and increased noise. As evident from Fig. 5-1 (a) there is little improvement in DQE(f) as thickness increases beyond 600 μm. The effect of both the thickness and beam energy on DQE is shown in Fig. 5-1 (b): DQE(f) decreases for higher kVp, mainly due to a decrease in interaction probability of higher energy photons, as expected from lower absorption coefficient .

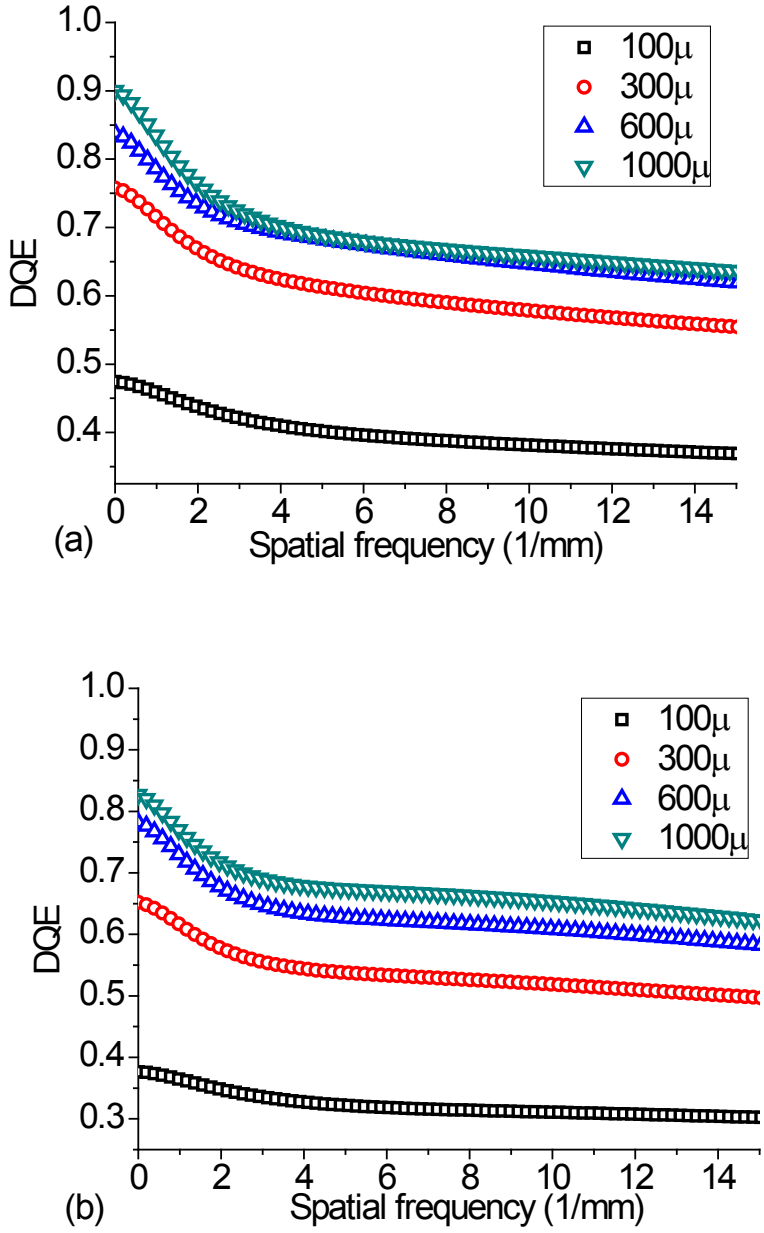

Fig. 5-1 (a) DQE(f) for 80 kVp; (b) DQE(f) for 120 kVp.

To summarize the trends in energy absorption with thickness and kVp we plot in Fig. 5-2 DQE(0) values obtained from DQE(f) analysis. Here we clearly observe the increase in the absorption efficiency of the detector with increasing thickness, becoming very moderate after 600 μm, especially for lower energies. For example, for 80 kVp, DQE(0) of 300 μm CdTe is about 59.7% more of that of 100 μm, however, the

DQE(0) of 1000 μm is only about 7.4% more than that of 600 μm.

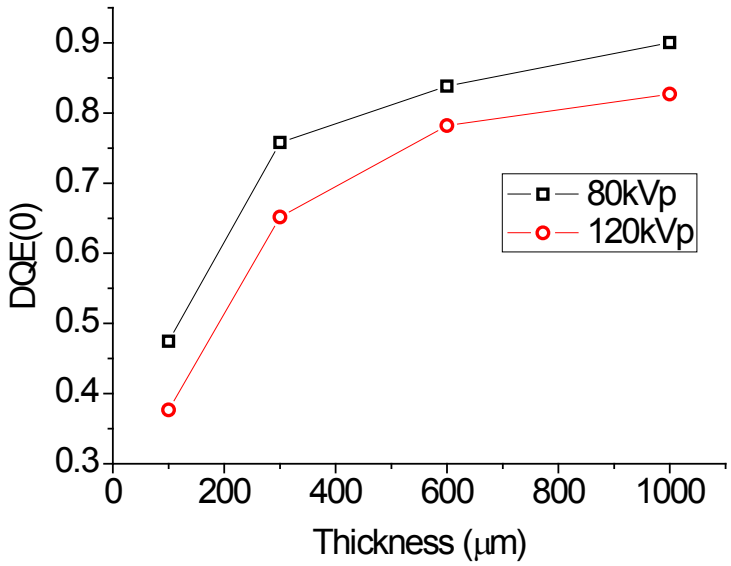

Fig. 5-2 DQE(0) of CdTe detector vs. the film thickness for different diagnostic X-ray spectra.

At the same time, the increase in number of X-rays having higher energies at higher kVp (Fig. 2-3) leads to decrease in DQE(0) for a given CdTe thickness. As the energy increases, the proportion of Compton interaction increases, and the fraction of energy transferred to the recoil electrons within the detector becomes much more variable than in a photoelectric interaction. Furthermore, the range of scattered photons and recoil electrons can be larger than the detector dimension, allowing a larger fraction of the transferred energy to escape.

5.3 DQE comparison analysis

The final DQE(f) calculated for the three materials are shown in Fig. 5-3 for two

spectra, 80 and 120 kVp. The latter spectrum produces the highest DQE for CdTe for frequencies f=0.4 and above. For example, at f=10, still within practical interest for kV imaging applications, DQE values for CdTe, HgI_2, and a-Se are 0.52, 0.45, and 0.31, respectively.

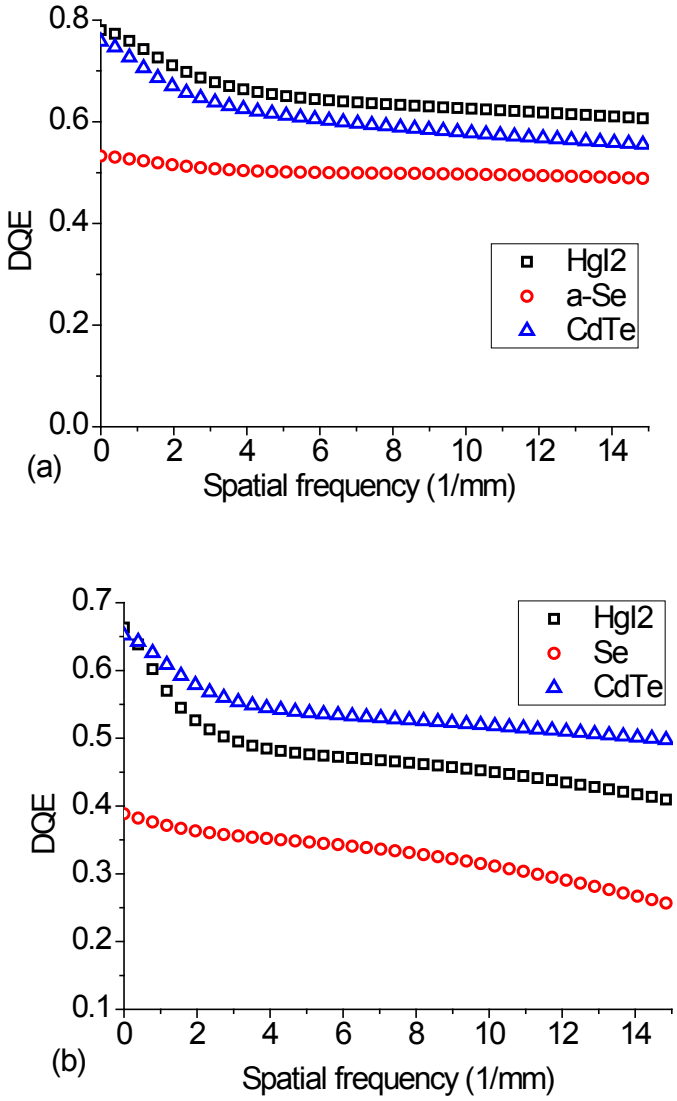

Fig. 5-3 DQE(f) of three photoconductors with a thickness of 300 μm (a) for 80 kVp beam; (b) for 120 kVp beam.

To verify the simulation results, we compared the DQE results with those published previously. The maximum measured DQE value of 0.7 for 350 μm thick CdZnTe was obtained in the study of S. Tokuda, et al. [29] for a 70 kVp beam. This is close to the

DQE(0) OF 0.76 calculated in this work under similar conditions (80 kVp, 300 μm thickness).

The value of DQE(0) for 300 μm thick a-Se for 80 kVp spectrum of our simulation is ~0.53. In the study of Zhao et al,[144] the calculated DQE(0) of 300 μm for a spectrum of 70 kVp is about 0.6 due to the Swank factor[83] and the broad X-ray spectrum using the cascade system model. These two values are quite close, taking into account the differences in calculation approaches and the input spectra. Du et al, [19] studied physical vapor deposition (PVD) polycrystalline HgI_2 with thicknesses ranging from 210 μm to 300 μm for an X-ray spectrum of 72 kVp. Their theoretical DQE(0) of 210 μm thick HgI_2 prototype calculated with cascaded system is about 0.6, t aking quantum efficiency and Swank factor into account. This is also close to our calculated DQE(0)=0.78 for 300 μm HgI_2 for 80 kVp, taking into account corrections for the thickness and spectra differences.

5.4 Conversion gain

The next part of analysis involves assessing the gain associated with conversion of the energy deposited by X-rays into electron-hole pairs in CdTe. This stage is termed the amplification stage in the multi-stage (cascaded) linear systems theory.[84] To evaluate this gain we use the energy required for creating one electron-hole pair in CdTe, W_{CdTe}~5 eV for polycrystalline material[85,86,87] (this value is very close to 4.43 eV measured for crystalline CdTe).[88] The amount of energy deposited in CdTe per

incoming X-ray is defined by the mean signal value A_0, and therefore depends on CdTe thickness. The maximum amplification gain g can be estimated as

$$g = \frac{A_0}{W_{CdTe}} \qquad (5\text{-}2)$$

and represents the upper limit estimate for the number of electron-hole pairs generated in a certain volume of CdTe.

Based on the energy deposition modeled with MC and using Eq. (5-2) we estimate the average number of electron-hole pairs created in the CdTe layer per 1 cm^2 area of the detector. The resultant dependences of generation rates on the CdTe thickness are shown in Fig. 5-4, where a log-log scale is used for clarity. The dependence is close to (1-exp (-at)) up to the CdTe thickness t of the order of the average X-ray penetration depth, saturating for thicker films.

Here we can also consider the noise associated with the gain variance that can be estimated based on the number of electron-hole pairs created N and Fano factor F (~0.1 for most semiconductors) as $\sigma_g \sim \sqrt{FN}$.[89] The resulting relative gain variance is $\sigma_g / g \leq 2\%$ for thicknesses of CdTe of 100 μm or larger.

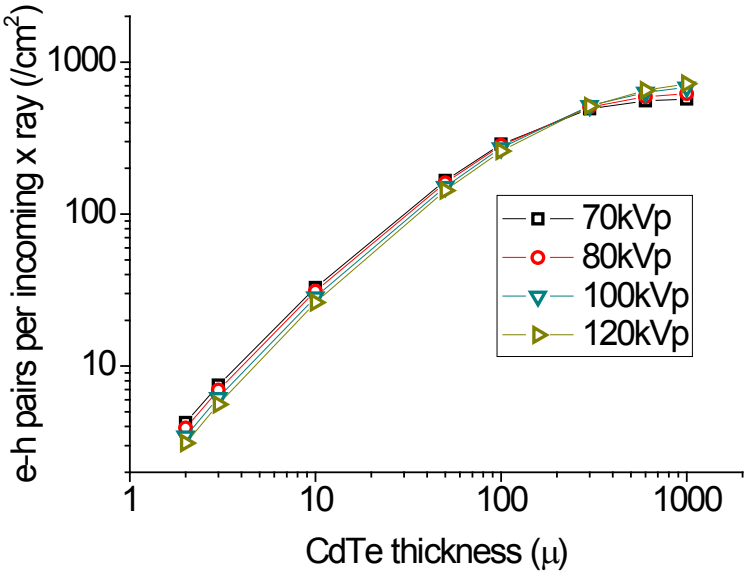

Fig. 5-4 Electron-hole pair generation per incoming X-ray over 1 cm^2 area of the CdTe detector for different diagnostic X-ray spectra.

5.5 Photon transport with Monte Carlo simulation

Monte Carlo simulation is a flexible yet powerful approach to model photon transport in media. In this type of simulation, photon propagation rules are expressed as probability distributions which describe the step size of photon movement between sites of photon-medium interaction, and the deflection angle in the trajectory of a photon when a scattering event occurs. This is equivalent to modeling photon transport analytically by the radiative transfer equation, which describes the motion of photons using a differential equation. However, close-form solutions of the radiative transfer equation are not always possible. Using diffusion approximation to simplify the radiative transfer equation may introduce many inaccuracies, especially near sources and boundaries. To the contrary, Monte Carlo simulations can achieve arbitrary

accuracy by increasing the number of photons traced. In addition, Monte Carlo simulations can keep tracking multiple physical quantities simultaneously, with any desired spatial and temporal resolution.

Photon transport in CdTe was simulated with MCNP5 Monte Carlo simulation software in this study. The modulation transfer function (MTF), noise power spectrum (NPS), and detective quantum efficiency (DQE) of the CdTe image detector were investigated by studying the energy deposition resulting from the simulated photon transport. The interaction details in the photon transport process in the Monte Carlo simulation are discussed next.

When a diagnostic X-ray travels through the CdTe, it generates secondary electrons through photoelectric effect, and Compton interactions; secondary electrons with enough energy will generate secondary photons. Detailed secondary electron and photon generation rates per incoming photon in CdTe under different spectra are summarized in Table 5-1. As we can see, with the increase of incoming photon energy, more secondary electrons are generated, explaining the increases in NPS with the potential energy. The number of secondary electrons, generated by C ompton recoil increasing with energy; while the number of photoelectrons decreases, consistent with changes in the corresponding interaction cross-sections for different energies. With the increase in the energy per incoming photon, more secondary photons are generated by bremsstrahlung resulting from the increased secondary electrons. The total secondary photons do not necessarily increase with the incoming photon energy, but more secondary photons will escape as the energy of incoming photon increases, explaining

why the DQE(0), the absorption efficiency, decreases with the increase in the potential energy.

Table 5-1 Generation of secondary electrons and photons for per incoming photon under different spectra.

Generated electron	70kVp	80kVp	90kVp	100kVp	110kVp	120kVp
Compton recoil	6.91E-03	8.13E-03	9.17E-03	1.00E-02	1.09E-02	1.16E-02
Photo-electric	1.17	1.18	1.17	1.16	1.15	1.13
Photon auger	5.94E-02	6.28E-02	6.46E-02	6.55E-02	6.57E-02	6.54E-02
Electron auger	1.14E-05	1.37E-05	1.79E-05	2.32E-05	2.27E-05	2.65E-05
Knock-on	3.36	3.62	3.80	3.92	4.02	4.09
Total	4.60	4.86	5.04	5.16	5.25	5.30
Escape	1.24E-04	1.76E-04	2.24E-04	2.67E-04	3.19E-04	3.71E-04
Energy cutoff	4.60	4.86	5.04	5.16	5.25	5.30
Generated photons						
Bremsstrahlung	1.32E-02	1.44E-02	1.53E-02	1.60E-02	1.65E-02	1.70E-02
Electron X-ray	5.07E-05	7.11E-05	9.23E-05	1.09E-04	1.27E-04	1.40E-04
1^{st} fluorescence	0.53	0.54	0.55	0.55	0.55	0.54
2^{nd} fluorescence	2.79E-02	2.89E-02	2.93E-02	2.94E-02	2.93E-02	2.90E-04
Total	1.57	1.59	1.59	1.60	1.59	1.59
Escape	0.26	0.28	0.29	0.30	0.32	0.33
Captured	1.31	1.31	1.30	1.29	1.27	1.26

Generation of the secondary electrons and photons increase with the detector thickness; however, their increasing magnitude decreases with the thickness increase. This is consistent with Fig. 5-2, where DQE (0) increases with thickness, but the rate of this increase decreases for thicker detectors. The secondary electrons generated by Compton recoil and photoelectric interaction increase with the detector thickness, and fewer secondary electrons escape for thicker detectors, explaining the NPS increases with detector thickness. Also, with the increase of detector thickness, more secondary photons are generated by bremsstrahlung and fluorescence; this is well presented by

the decrease of MTF with the detector thickness in Fig. 3-4 (a).

Table 5-2 Generated secondary electrons and photons per incoming photon for different thickness of CdTe detector.

Generated electrons	100μm	300μm	600μm	1000μm
Compton recoil	4.07E-03	6.87E-03	8.13E-03	8.63E-03
Photo-electric	0.60	1.03	1.18	1.22
Photon auger	3.50E-02	5.56E-02	6.28E-02	6.52E-02
Electron auger	1.01E-05	1.18E-05	1.37E-05	1.44E-05
Knock-on	1.69	3.07	3.62	3.80
Total	2.33	4.17	4.86	5.09
Escape	2.06E-04	1.85E-04	1.76E-04	1.74E-04
Energy cutoff	2.33	4.17	4.867	5.09
Generated photons				
Bremsstrahlung	6.67E-03	1.22E-02	1.44E-02	1.52E-02
Electron X-ray	2.98E-05	5.67E-05	7.11E-05	7.70E-05
1^{st} fluorescence	0.30	0.48	0.54	0.56
2^{nd} fluorescence	1.61E-02	2.57E-02	2.89E-02	2.99E-02
Total	1.32	1.52	1.59	1.61
Escape	0.65	0.37	0.28	0.25
Captured	0.67	1.15	1.31	1.29

Statistics of secondary electron and photon production for three different materials, Se, CdTe and HgI_2, with a thickness of 300 μm for 80 kVp and 120 kVp spectra are summarized in Table 5-3. Because the K-edges of Cd and Te are very close to the mean energy of 80 kVp spectrum, many more secondary electrons are generated in CdTe than Se and HgI_2 per incoming photon through the photoelectric effect, which also results in more knock on electrons. As the mean energy of the incoming spectrum increases, the photoelectric coefficients of Se and CdTe decrease, and fewer secondary electrons are generated. To the contrary, the production of secondary electrons through photoelectric interactions in HgI_2 increases as the mean energy gets close to the K-edge of Hg as indicated in Fig 1-1, therefore more electrons were generated in HgI_2 for 120 kVp.

The generated photons in Se under these two energies are fewer in number than those in CdTe and HgI_2. The proportion of fluorescence photons in Se is much lower than that of CdTe or HgI_2; this result is consistent with the MTF results in Fig. 3-5, where Se has a higher spatial resolution than CdTe and HgI_2. However, the proportion of escaped secondary photons in Se is much higher than that of CdTe and HgI_2, which indicates lower absorption efficiency. This explains the lower DQE (0) of Se compared to both CdTe and HgI_2 under these two energies. The total number of generated secondary photons decreases for Se and CdTe from 80 kVp to 120 kVp; while for HgI_2, more photons are generated as the energy increases from 80 kVp to 120 kVp, due to increased absorption coefficients of HgI_2 after its K-edge, as shown in Fig. 1-1.

Table 5-3 Generated electrons and photons per incoming photon in three different materials with a thickness of 300 μm for 80 kVp and 120 kVp spectra.

Materials	Se		CdTe		HgI2	
Generated electrons	80 kVp	120 kVp	80 kVp	120 kVp	80 kVp	120 kVp
Photo-electric	0.60	0.28	1.03	0.63	0.63	0.82
Knock-on	1.80	1.11E-03	3.07	2.48E-03	1.61E-03	2.52E-03
Total	2.52	0.28	4.17	0.69	0.63	0.83
Escape	1.38E-04	1.13E-04	1.85E-04	3.02E-04	1.87E-04	2.85E-04
Energy cutoff	2.52	0.28	4.17	0.69	0.63	0.83
Generated photons						
Bremsstrahlung	5.53E-03	9.43E-04	1.22E-02	2.23E-03	2.42E-03	2.96E-03
1st fluorescence	0.13	0.077	0.48	0.43	0.34	0.41
Total	1.14	1.08	1.52	1.43	1.34	1.41
Escape	0.54	0.73	0.37	0.46	0.34	0.42
Captured	0.60	0.35	1.15	0.98	1.01	0.99

Chapter 6

Modeling of Device Performance with SCAPS Simulation

A thin film photovoltaic device (PV) has a very simple structure. However, calculation of the device characteristics based on the parameters of the materials constituting a device can be very involved. A variety of measurements have been presented in the literature with the aim of obtaining information on optical and electronic properties of these devices. However, since most of the experimental characterization techniques were developed for crystalline semiconductors, interpretation of these measurements for thin films is often difficult. Certain assumptions and simplifications are required for numerical modeling of thin film PV devices operations.

Due to the presence of the junction with cadmium sulfite (CdS), our polycrystalline CdTe detector can function in a photovoltaic mode, without application of the external bias. While there are similarities in operations of a solar cell and X-ray detector, the main difference arises from orders of magnitude higher energies of the incoming beam in the latter case, resulting in the requirement of much thicker semiconductor layer for the adequate signal registration. However, these similarities with PV devices allowed us to employ the device simulation software package, SCAPS-1D (solar cell capacitance simulator),[90,91] typically used for solar cell modeling, to investigate the performance of our proposed thin film CdTe X-ray detector.

The typical operation of a semiconductor detector is based on collection of the

charges (electron-hole pairs), generated by photon interactions. The charge separation is facilitated by the internal built-in filed, or through the application of an external electric field. For diagnostic X-ray beam range, the most important interaction mechanisms are photoelectric absorption and Compton scattering. In photoelectric absorption the photon transfers all its energy to an atomic electron, while a photon interacting through Compton process transfers only a fraction of its energy to an outer electron, producing a hot electron and a degraded photon. By studying the energy transfer and deposition during these interactions, we were able to obtain electron hole generation profiles under realistic X-ray beams. These profiles were used as inputs for SCAPS device simulation software, thus allowing characterization of the electronic performance of detectors with a numerical modeling.

6.1 Monte Carlo simulation of energy transfer and deposition

The principle of photovoltaic operation mode of CdTe under X-rays is schematically shown in Fig. 6-1 (a). As an X-ray is absorbed in the detector, a number of electron hole pairs are directly generated. These electron hole pairs will be separated and collected due to the built-in electric field. By analyzing the collected output signal, open circuit voltage (Voc) and short circuit current (Jsc), the electronic characteristics of thin film CdTe under diagnostic X-ray beam could be assessed. After measuring the output of the Varian Ximatron simulator by Unfors electrometer, the diagnostic X-ray spectra of this simulator were obtained by tungsten anode spectra modeling using

interpolating polynomial (TASMIP) method,[53] as shown in Fig. 2-3.

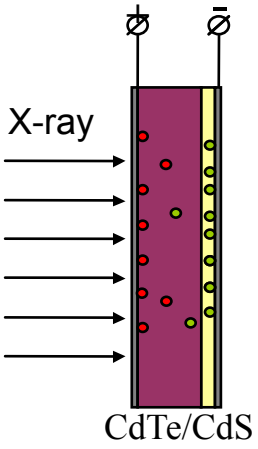

Fig. 6-1 Photovoltaic operation model of thin film CdTe detector.

Monte Carlo simulations with the MCNP5 package were employed to obtain the energy deposition profiles of diagnostic X-rays incident on t he thin film CdTe. Modified pulse-height tally *F8 was used to obtain the energy deposition through the film, subdivided into lattice cells along the film depth. In all simulations, the electron cut-off energy (ECUT) was chosen so that the electron range at ECUT is less than 1/3 of the smallest dimension in the dose scoring region,[59,60] 0.01 MeV for 1 micron depth increments. The cut-off energy for photons was set to 0.01 MeV, with coherent, photonuclear and Doppler interactions turned off.

The energy deposited (in MeV/photon) in each lattice volume of the CdTe detector simulated by the Monte Carlo simulation is presented in Fig. 6-2 for 10 μm, 100 μm, and 300 μm. As we can see, for 10 μm and 100 μm CdTe detectors, the energy deposited is decreased with the increase of incoming energy. This is due to the decrease in probability of photoelectric interaction with the increase in energy. As the thickness increases, secondary electrons have more chances to deposit their energy passed the

photon penetration depth instead of escaping, so more energy will be deposited for high potential beams, as we can see from the end part of Fig. 6-2 (b) and Fig. 6-2 (c).

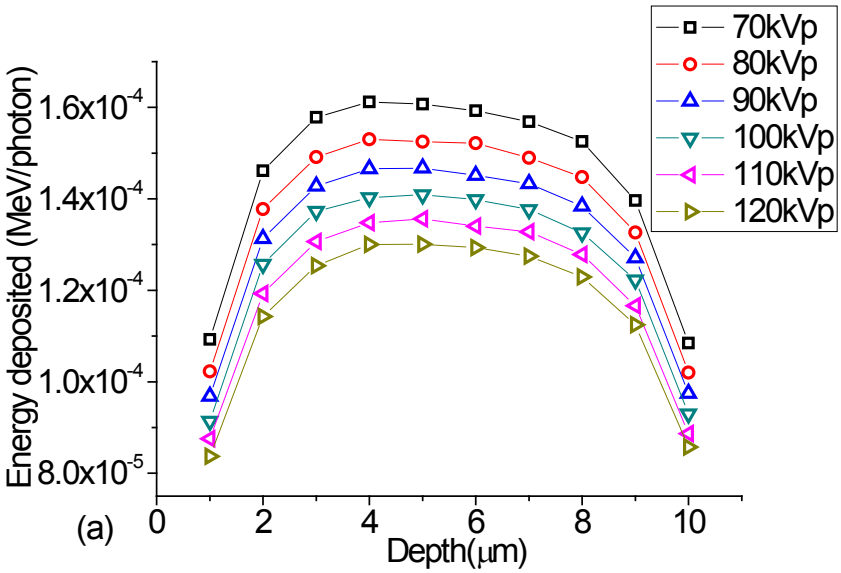

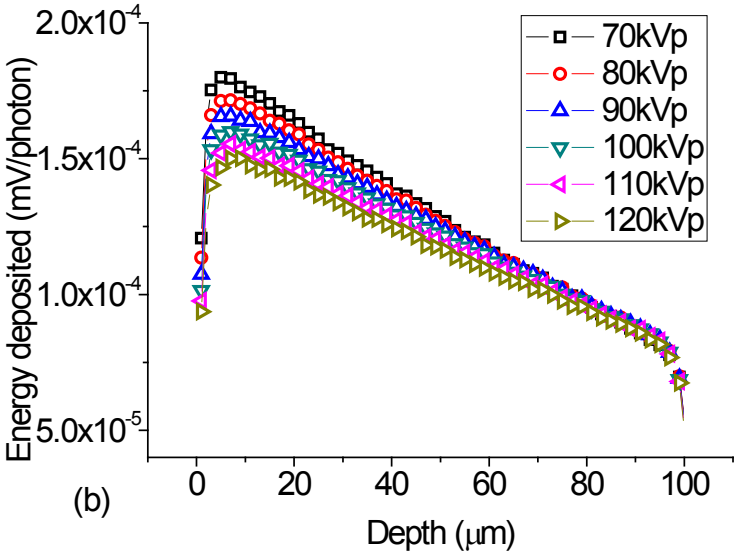

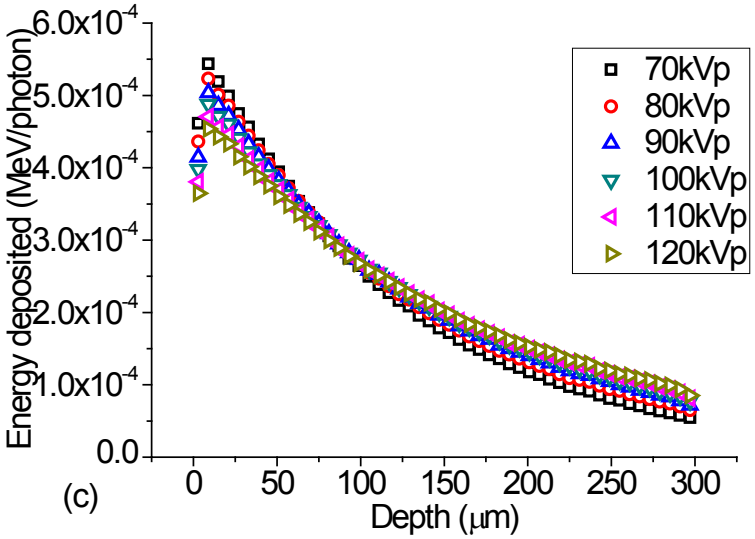

Fig. 6-2 Simulated energy deposition per incoming photon in thin film CdTe for (a) 10 μm; (b) 100 μm; and (c) 300 μm.

6.2 Electron hole pair generation profiles

In order to adapt to the format of generation profiles used in the SCAPS simulation software,[90,91] we need to calculate the electron hole pairs generated per mm^3 per second in the CdTe. The electron hole pairs generated on each layer of CdTe were calculated based on the above energy deposition.

First, by converting the deposited energy to eV/photons and dividing by the effective ionization energy 4.43 eV,[88,92] the energy required to generate one electron hole pair, we can calculate the electron hole pairs generated per mm^3 per incoming photon.

$$(\frac{MV}{photon}\times\frac{10^6\,eV}{MV})/(mm^3\times 4.43eV)=\frac{e-h\quad pairs}{mm^3\,photon} \qquad (6\text{-}1)$$

Fig. 6-3 is the measured radiation output of the Varian Ximatron simulator at

different tube currents for different energies. Combined with the simulated spectra in the Fig. 2-3, we can calculate the coming photon fluence rate for different tube currents:

$$\frac{photons}{mm^2 mR} \times \frac{mR}{s} = \frac{photons}{mm^2 s} \qquad (6\text{-}2)$$

So for certain area (mm^2) of thin film detector, we can obtain the electron hole pairs generation rate per volume per second for different energy and different tube currents

$$\frac{e-h \quad pairs}{mm^3 \, photon} \times \frac{photons}{mm^2 s} \times mm^2 = \frac{e-h \quad pairs}{mm^3 s} \qquad (6\text{-}3)$$

The resultant electron hole pair profiles along the path of the beams in the CdTe detector are the generation profiles required for SCAPS simulation. As shown in Fig. 6-4, for different thickness of CdTe for the same energy and tube current, the electron hole pair generation profiles follow the trend of energy deposition calculated via Monte Carlo simulation. For the same energy but a different tube current, the number of electron hole pairs increases with the increase of tube current, as shown in Fig. 6-4 (b). This is because the intensity of the incoming photons is proportional to the tube current, more incoming photons, more energy deposited. The number of electron hole pairs also increases with the tube potential (kVp) under the same tube current, as shown in Fig. 6-4 (c). This is also due to the increase in the number of incoming photons, as well as increase in the average photon energy. This trend is consistent with results shown in Fig. 6-3, where the rate of energy deposition (the dose rate) increases with the beam energy.

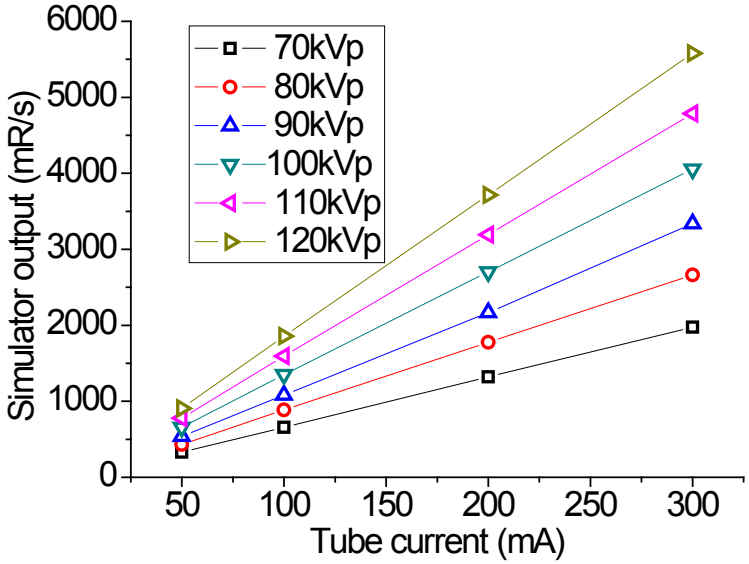

Fig. 6-3 Measured output dose rate of Varian Ximatron simulator under different tube current for different beam energies, defined by the tube potential (kVp).

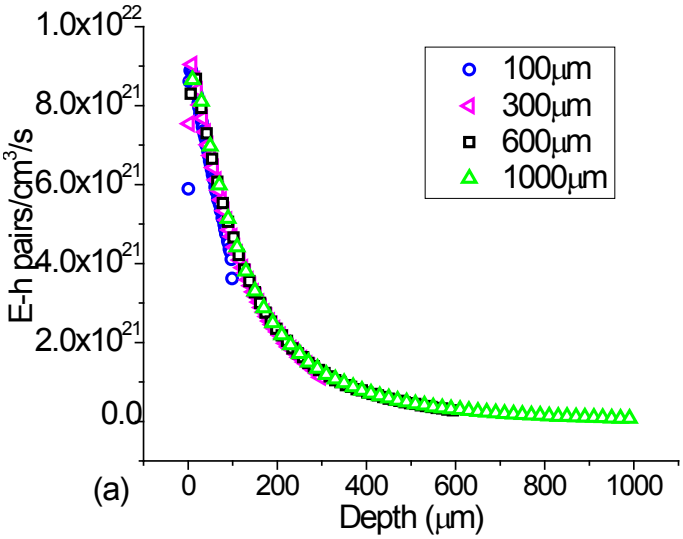

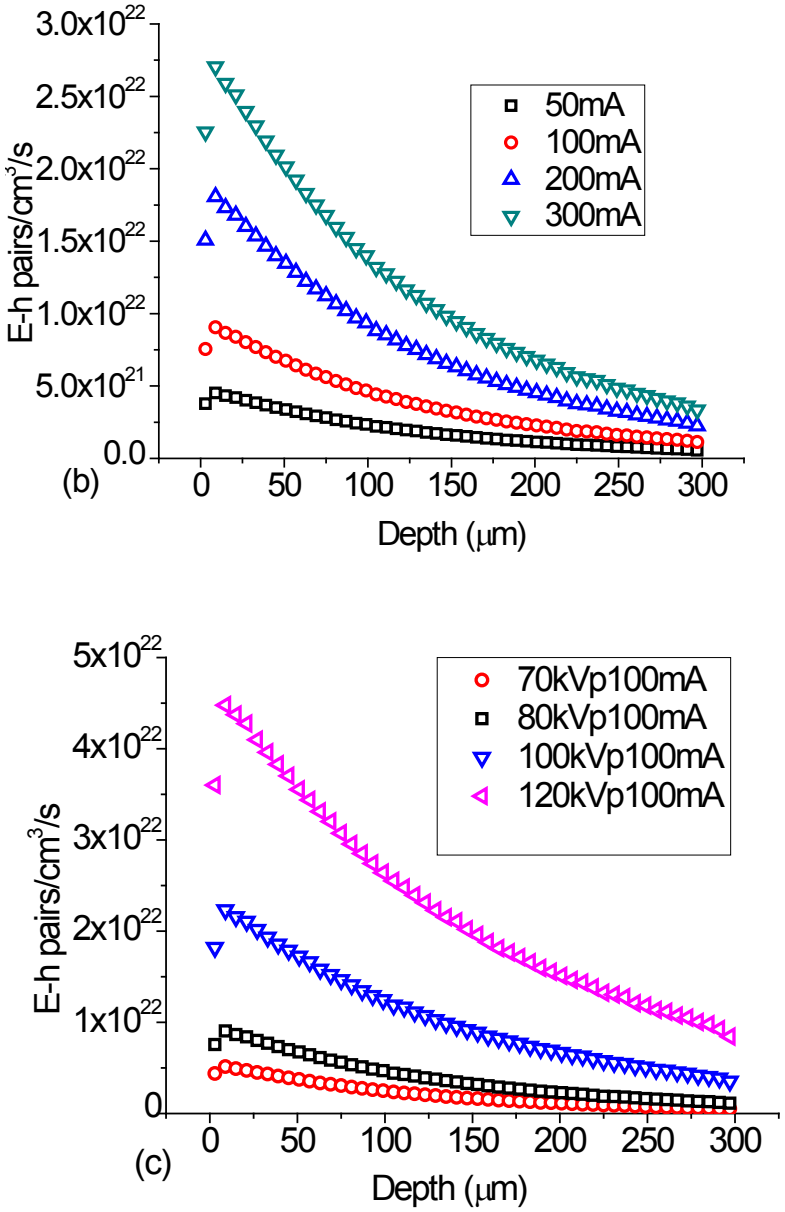

Fig. 6-4 Electron-hole pair generation profiles for (a) different thickness CdTe for 80 kVp 100 mA; (b) for 300 μm thickness CdTe under different tube current at 80 kVp; (c) for 300 μm thickness CdTe under 100 mA tube current of different energy.

6.3 Device operation with SCAPS

To characterize the detector operation, we use the SCAPS-1D software package, originally developed for thin film solar cells modeling. The software is designed to

take an optical spectrum together with absorption coefficient information, or charge carrier generation profile, as input and calculate current-voltage (I-V), capacitance-frequency, or spectral response characteristics of a device specified as a stack of several layers of different materials.[93] Each layer is characterized through a set of parameters such as effective density of states, thermal velocity, band-gap, and mobilities.

Since both thin film solar cell and detector system have essentially the same principle of operation, we used a baseline model for CdTe/CdS solar cell[94] as a starting point. The main differences of our detectors from a typical solar cell are the much larger thickness and the shape of the charge carrier generation profile. For its application in diagnostic X-ray, the thickness of CdTe detector should be much thicker than its solar cell device, which is typically of 3 to 5 μm thick, in order to achieve adequate X-ray absorption. It has been reported that crystalline detectors having thickness of 1-2 mm often suffer from low hole mobility, imposing the necessity of a large (about 100 to 1000 volts) bias voltage application across the device.[95] Since the thickness of our proposed polycrystalline CdTe device is much thinner, we expect reasonable output signal without biasing, relying on built-in junction field, found in a typical CdS/CdTe solar cell. The value of this field is about 10^4 V/cm,[96] similar to the field strength obtained with external biasing for detector application.

The basic equations utilized in the software SCAPS are the Poisson equation, relating the charge to the electrostatic potential Φ, and the continuity equations for electrons and holes.[97]

$$\nabla \cdot \varepsilon \nabla \Phi = -q(p - n + N_{D+} - N_{A-})$$
$$\nabla \cdot J_n = q(R - G) + q\frac{\partial n}{\partial t}$$
$$-\nabla \cdot J_p = q(R - G) - q\frac{\partial p}{\partial t} \qquad (6\text{-}4)$$

Where ε is the dielectric constant, Φ is the electrostatic potential, q is the electron charge, n and p are the free carrier concentrations, N_{D+} and N_{A-} are the density of ionized donor and acceptor levels, J_n and J_p are the electron and hole current density, R is the recombination rate , and G is the generation rate.

The recombination terms included in the continuity equations make the problem nonlinear. Shockley-Read-Hall (SRH) formalism was applied to describe the recombination in deep bulk levels and their occupation.[98] Recombination at the interface states is described by an extension of SRH formalism, allowing the exchange of electrons between the interface state and the two adjacent conduction bands, and of holes between the state and the two adjacent valence bands.[99]

After the device structure is completely specified the simulation procedure in SCAPS is straightforward. By setting up the thickness of CdTe layer, the current-voltage characteristics under different potential energy and tube current of diagnostic X-ray beams can be calculated by using above charge carrier generation profiles as inputs.

6.4 Simulation results

The diode current-voltage (I-V) characteristics of the detector is

$$I = I_{sc} e^{\frac{e(V-Voc)}{kT}-1} \qquad (6\text{-}5)$$

where I_{SC} is the saturation current, Voc is the open-circuit voltage, e is the electron charge, k – Boltzmann's constant, and T is the device absolute temperature. According to this equation the current change is linear with energy deposition (and number of photons in the beam) while the voltage increase is logarithmic. This agree with SCAPS simulation results, shown in Fig. 6-5, where Voc and Jsc parameters are presented for CdTe detectors of different thickness for 80 kVp spectrum. Fig. 6-5 (a) indicates the Voc increases as a logarithm of the tube current, while Jsc (short circuit current density at V=0) increases linearly with an increase of the tube current.

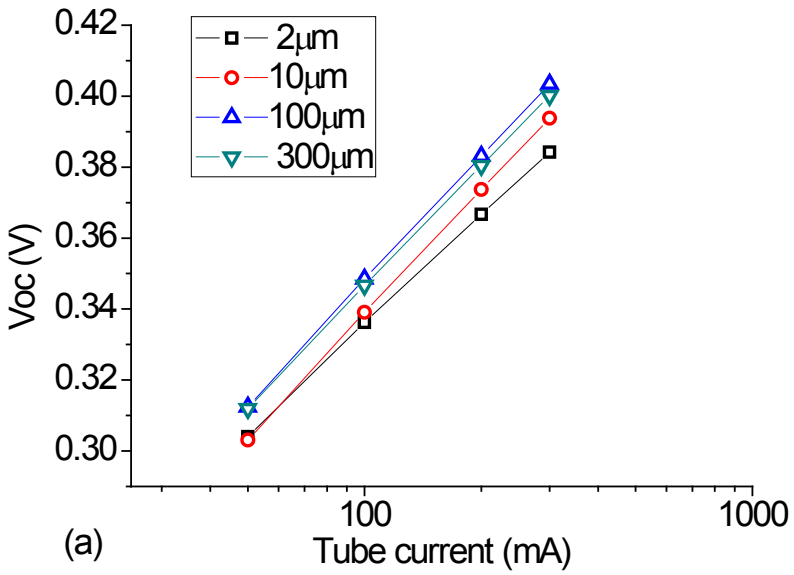

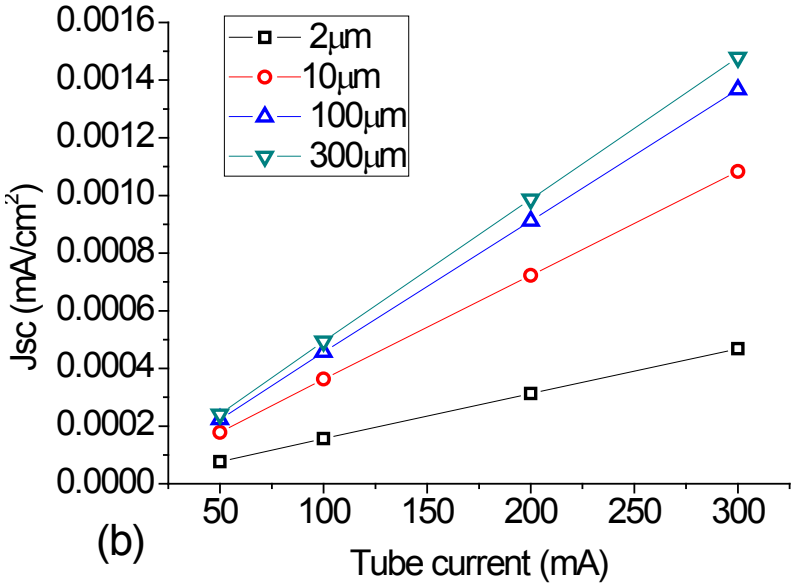

Fig. 6-5 SCAPS simulation results of CdTe detectors for 80 kV p with different thickness as a function of tube current (a) open circuit voltage, Voc; (b) short circuit current density, Jsc.

For different thickness of CdTe detectors, the output signal increases with an increase of thickness for thinner film. This is because with an increase of thickness, more photons interact within the detector, and more energy is absorbed. From the energy deposition curve above obtained by Monte Carlo simulation, we found that the penetration depth of diagnostic X-ray beams in CdTe is around 150 μm. So beyond this thickness, the rate of energy absorption increase is decreased. As we can see from Fig. 6-6 (b), the short circuit current density is almost flattened after 300 μm. Fig. 6-6 (a) indicates similar trend for open circuit voltage, although having a bump at 600 μm thickness. The latter is probably caused by a deficiency of the simulation software itself, which was originally optimized for thin film devices.

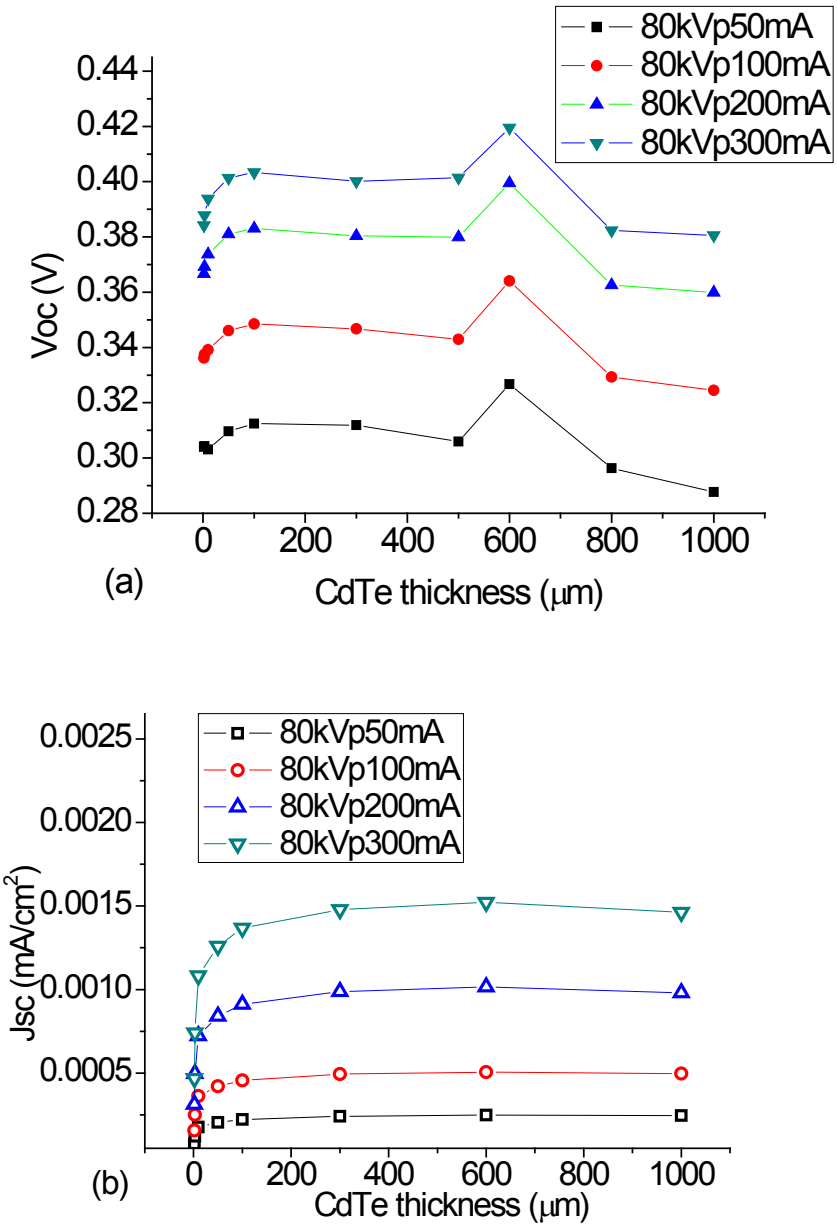

Fig. 6-6 SCAPS simulation results of CdTe detectors as a function of detector thickness (a) Voc; (b) Jsc for 80 kVp.

The output signal also increases with the potential energy of the incident photons. With the increase of the tube potential, the total number of photons, as well as their average energy increases, as evident from the spectra in Fig. 2-3, where the area under high kVp spectra is greater than that of the lower ones, so more energy is available for absorption from the high kVp beams. But the signal increase is sharper for thicker

films, as shown in Fig. 6-7 (b). This is due to the increase of absorption with the increase of film thickness.

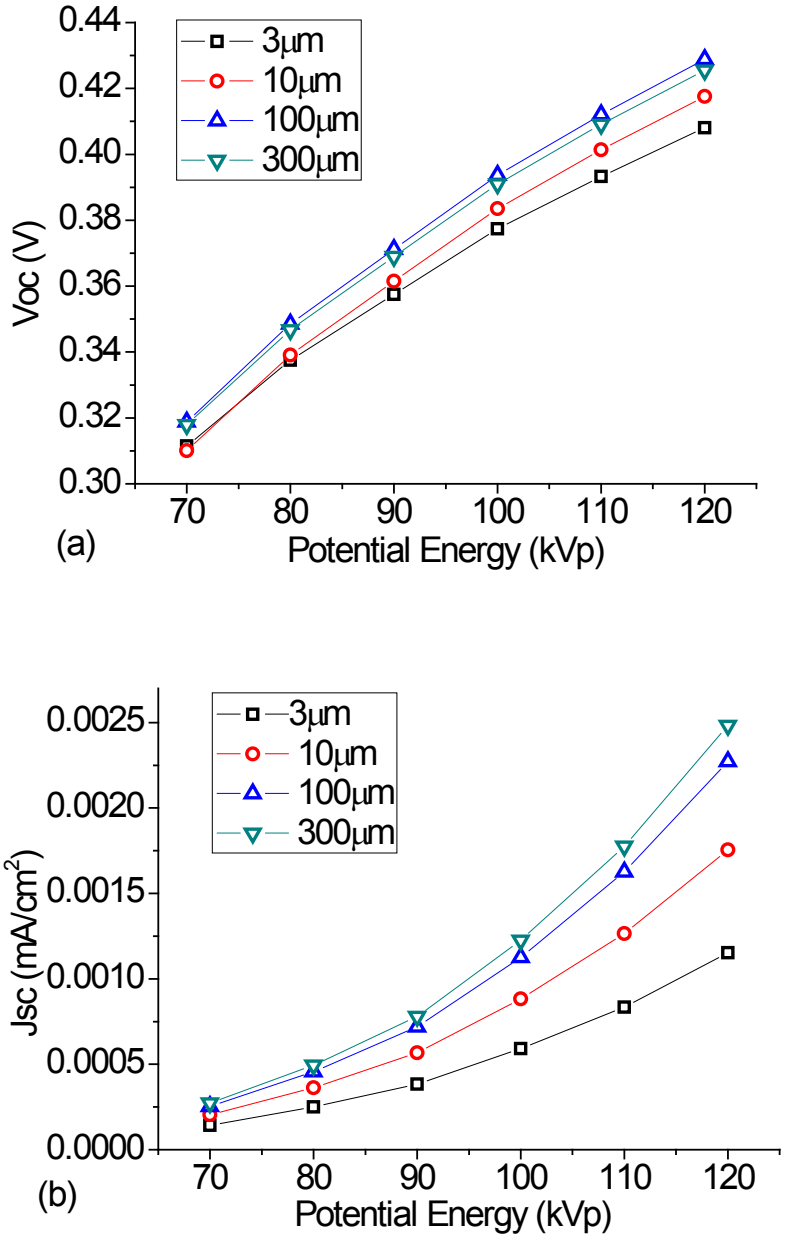

Fig. 6-7 SCAPS simulation results of CdTe detectors as a function of potential energy (a) Voc; (b) Jsc.

Chapter 7

Experimental Measurement

Due to the high atomic number, the high density and the wide band gap, CdTe and CdZnTe detectors ensure high detection efficiency, good room temperature performance, and are very attractive for X-ray and gamma ray applications.[100,101] The main difficulty that limits CdTe and CdZnTe for wide application lies in growing chemically pure and structurally perfect crystals used for thick detectors. This situation has changed dramatically during the last decades with developments in thin-film solar cell research.

In this chapter, by measuring the output signal, voltage and current for diagnostic X-ray beams, the electronic characteristics of polycrystalline CdTe based on detector sensitivity, linearity, and time response, will be studied and discussed.

7.1 The experimental methods

Photovoltaic detectors generate a measureable voltage and current in response to diagnostic X-ray bombardment, much like a solar cell (Fig. 7-1 (a)). Since their operation principle is the same, the same set of parameters were used to characterize the photovoltaic detector, such as open circuit voltage (Voc), the DC voltage produced by a photovoltaic detector under irradiation, and short circuit current (Isc), the current measured at voltage V=0.

Current-voltage relationship is normally used to characterize a device operation in an electronic circuit. In our study, CdTe detectors of 3 μm and 10 μm thickness were irradiated with the diagnostic X-ray spectra of Varian Ximatron simulator. Current and voltage are the two main parameters for PV device characterization. Its typical I-V curve was shown in Fig. 7-1 (b). Current-voltage measurements were performed with the Keithley electrometer (model 2636A) in 2-point probe setup. In order to compare the measurement results with SCAPS simulation, and to better understand the performance of much thicker detectors, such as 600 μm and 1000 μm, which are beyond our regular PV lab availability, no external bias was applied during the measurement. We relied on the built-in potential to collect the output signal instead.

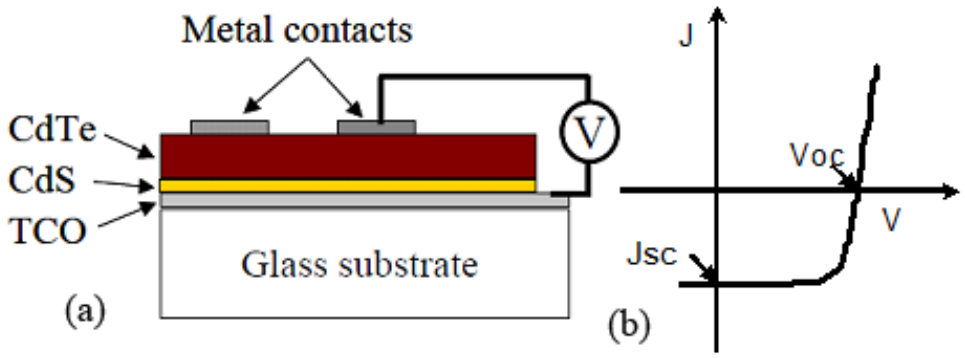

Fig. 7-1 (a) Sketch of a CdTe solar cell; (b) typical current-voltage curve of sunlight photovoltaic device under illumination.

.

The CdTe devices in this experiment, provided by N ational Renewable Energy Laboratory (NREL), had thickness of 3 μm and 10 μm. These devices were fabricated by the sequential deposition of SnO_2, CdS, CdTe, and a b ack contact layer on borosilicate glass (Corning 7059) substrates. Low pressure chemical vapor deposition[102] and chemical-bath deposition[103] were used to deposit the SnO_2 and CdS

layers, respectively. Low-temperature nucleation thermal profile during the close-spaced sublimation (CSS) process was used to grow CdTe on SnO_2/Corning 7059 glass substrates.[104] CdTe/CdS/SnO_2/Glass structures were then treated in vapor $CdCl_2$ at 400 ^{0}C to improve the efficiency of the solar cell.[105] Finally, a back contact consisting of a mixture of graphite paste and $Cu_{1.4}$Te+HgTe was applied and annealed in Helium at 280 ^{0}C. Ag-paste served as the final metal contact to the device.

7.2 Performance of the photovoltaic X-ray detector

The measurements were carried out to determine the sensitivity and linearity of the photovoltaic detectors under diagnostic X-ray beams. Thin film CdTe samples of 3 μm and 10 μm were irradiated with the Varian Ximatron simulator in the radiation oncology department at the University of Toledo Health Science Campus. Short circuit current and open circuit voltage under different conditions were measured.

All our experiments were performed with a field size of 20x20 cm^2 at a source to surface distance (SSD) of 90 cm. Due to the sensitivity of the solar cell to room light, the samples were wrapped in black cloth during measurement, and the room light was turned off. Different intensity diagnostic X-ray beams, specified by tube current (50, 100, 200, and 300 mA), for different kVp energy were applied to irradiate the thin film CdTe samples.

A set of typical measured I-V curves are shown in Fig. 7-2 for a 10 μm CdTe sample in the dark, as well as under 80 and 120 kVp beams. Short circuit current (Isc)

or current density (Jsc), and open circuit voltage (Voc) can be interpreted from the measured I-V curves. The sensitivity and linearity can be evaluated by analyzing the measured Isc and Voc. A total of 35 samples of 3 μm and 8 samples of 10 μm were measured, where only 20 of 3 μm and 5 of 10 μm samples gave reasonable output signals under diagnostic X-ray beams. This is a typical behavior of photovoltaic devices under low intensity illumination,[106] attributable to lateral non-uniformities within each device.

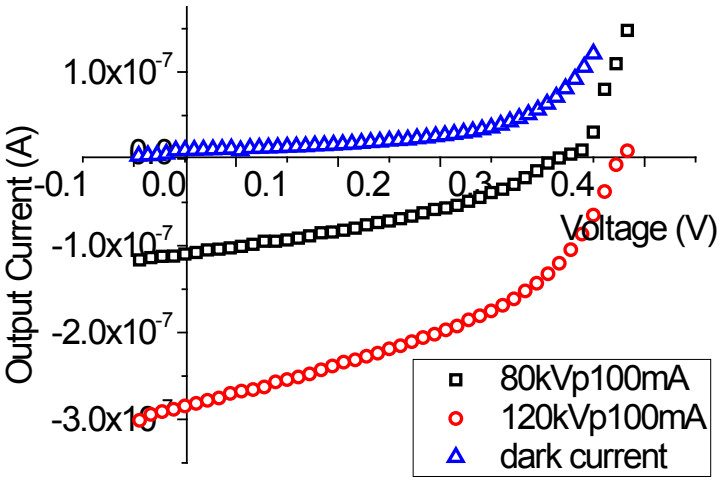

Fig. 7-2 Typical measured I-V curves of a 10 μm cell in the dark, under 80 kVp and 120 kVp beams.

The sensitivity of a detector can be defined in terms of the charge produced per incident X-ray quantum of a specified energy. The sensitivity depends on η and on the primary conversion efficiency, where $\eta = 1 - e^{-\mu(E)T}$ is the quantum efficiency. Conversion efficiency can be expressed in terms of the effective ionization energy, ω, necessary to release an electron-hole pairs in the detector. CdTe has a relatively small ω, ~ 5 eV, compared to that of a-Se, which is about 50 eV. This results the sensitivity of

CdTe about 10 times higher than that of a-Se.[107]

Fig. 7-3 shows the measured Jsc and Voc of 3 μm CdTe for two different energies. The output current increases linearly with the intensity and the potential of the X- ray beams, as shown in Fig. 7-3 (a). The measurement results for two thicknesses of samples performed for 80 and 120 kVp spectra are summarized in table 7-1 and table 7-2. Both thicknesses of detectors showed enough sensitivity and linearity under diagnostic X-ray beams. However, the measurement uncertainties also increase with the tube current and potential. The output voltage follows a logarithm relationship with the incident energy, as we mentioned in Chapter 6. This is demonstrated in Fig.7-3 (b), where increase of Voc with the tube current is shown in a semi-logarithm scale.

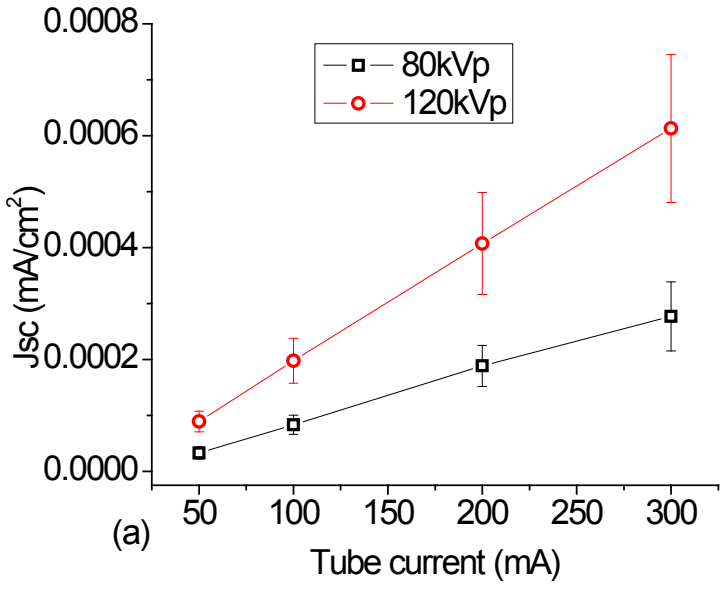

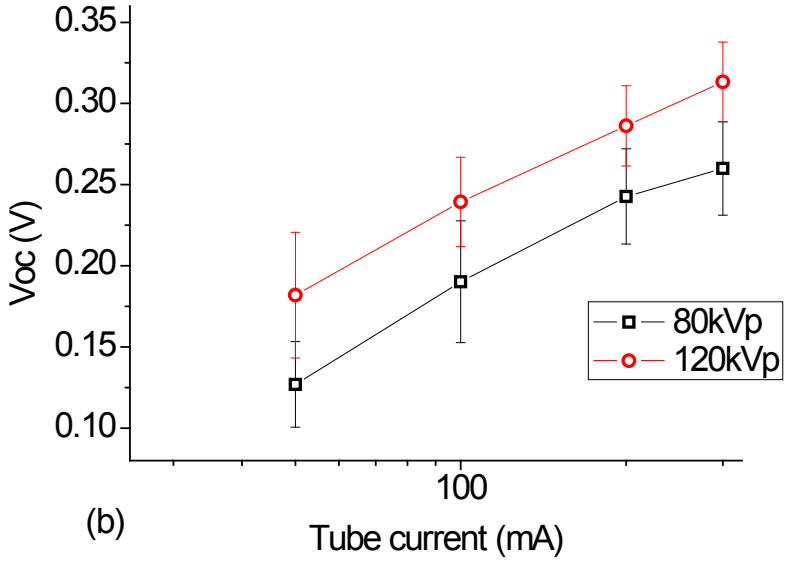

Fig. 7-3 Measured (a) short circuit current density (Jsc); and (b) open circuit voltage (Voc) of 3 μm CdTe for 80 and 120 kVp beams.

Table 7-1 Measured and simulated open circuit voltage (Voc) comparison.

Tuber current (mA)		50	100	200	300
3μm80k	Measured	0.13±0.026	0.19±0.037	0.24±0.029	0.25±0.029
Voc (V)	Simulated	0.25	0.28	0.31	0.33
10μm80k	Measured	0.14±0.076	0.21±0.059	0.26±0.058	0.29±0.0656
Voc (V)	Simulated	0.30	0.33	0.37	0.39
3μm120k	Measured	0.18±0.039	0.24±0.028	0.29±0.025	0.31±0.025
Voc (V)	Simulated	0.29	0.32	0.35	0.37
10μm120	Measured	0.24±0.054	0.29±0.056	0.32±0.061	0.34±0.062
k Voc (V)	Simulated	0.29	0.32	0.36	0.38

Table 7-2 Measured and simulated short circuit current density (Jsc) comparison.

Tuber current (mA)		50	100	200	300
3μm80k	Measured	3.27E-5	8.31E-5	1.88E-4	2.77E-4
Jsc		±1.07E-5	±1.69E-5	±3.68E-5	±6.17E-5
(mA/cm^2)	Simulated	8.67E-5	1.69E-4	3.31E-4	4.91E-4
10μm80k	Measured	2.47E-5	6.58E-5	1.55E-4	2.46E-4
Jsc		±2.41E-5	±4.12E-5	±8.16E-5	±1.21E-4
(mA/cm^2)	Simulated	1.62E-4	3.20E-4	6.35E-4	9.49E-4
3μm120k	Measured	8.89E-5	1.98E-4	4.07E-4	6.13E-4
Jsc		±1.83E-5	±4.03E-5	±9.13E-5	±1.32E-4
(mA/cm^2)	Simulated	8.99E-5	1.78E-4	3.54E-4	5.27E-4
10μm120k	Measured	8.80E-5	1.92E-4	4.02E-4	6.14E-4
Jsc		±4.98E-5	±9.55E-5	±1.90E-4	±2.76E-4
(mA/cm2)	Simulated	1.36E-4	2.68E-4	5.32E-4	7.95E-4

7.3 Comparison with simulated results

Tables 7-1 and 7-2 also show the comparison of the measurement results for 3 and 10 μm CdTe devices with those of SCAPS simulations. As we can see from Fig. 7-4, the output signal from simulation is relatively higher than the measured results, especially under lower tube current beams, corresponding to lower photon intensities. The discrepancy can be expected since the simulation models an idealized device, producing maximum output. It also points out to the need of self-consistent adjustment of the model parameters, especially for the case of an x-ray detector, operating at photon intensity level of a diagnostic X-ray beam, which is 5 orders of magnitude lower than that of 100 W/cm^2, corresponding to "one sun" intensity of the sunlight. The CdTe/CdS baseline model was built to simulate the device operation under the sunlight, with material parameters adjusted to match I-V characteristics of the best

solar cells. However, it does not take into account properties of realistic devices, especially evident at low light intensities. It has been reported that as the light intensity goes down, the variations in photovoltaic parameters increase,[106] the effect that cannot be easily incorporated into a 1-dimentional model.

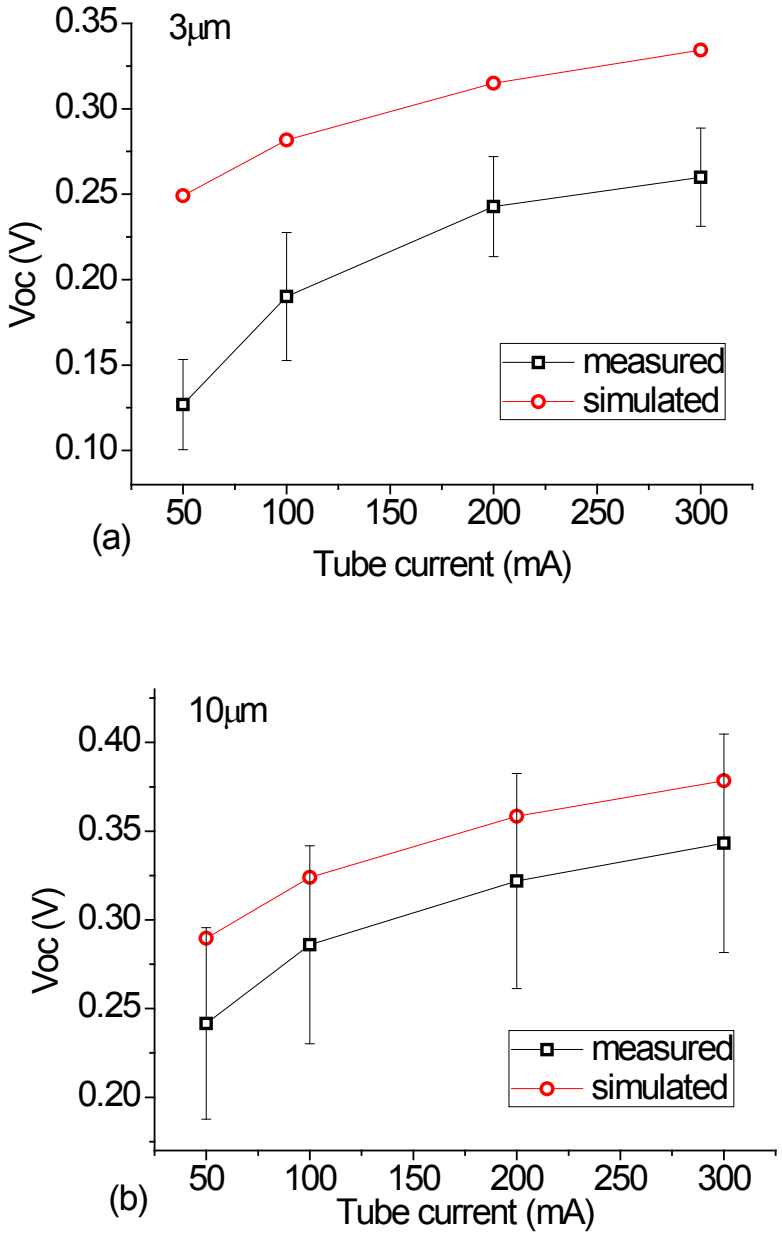

Fig. 7-4 Simulated and measured output signal comparison (a) Voc of 3 μm for 80 kVp; (b) Voc of 10 μm for 120 kVp.

To verify our prediction, output signals of our 10 μm samples under different levels of sunlight were measured. The low intensity light was obtained by blocking the light source, simulating the sun with various gray and black sheets. The resulting light intensity was measured with a standard silicon solar cell in the lab.

As clearly indicated in Fig. 7-5, below 2e-5 sun light, both signals, Voc and Jsc, start to depart from a linear relationship. The diagnostic X-ray beam intensity is around 1e-5 of one sun. Therefore these data support the explanation for the discrepancies between simulated and measured results. Indirectly, they may also account for the large error bar during the measurement.

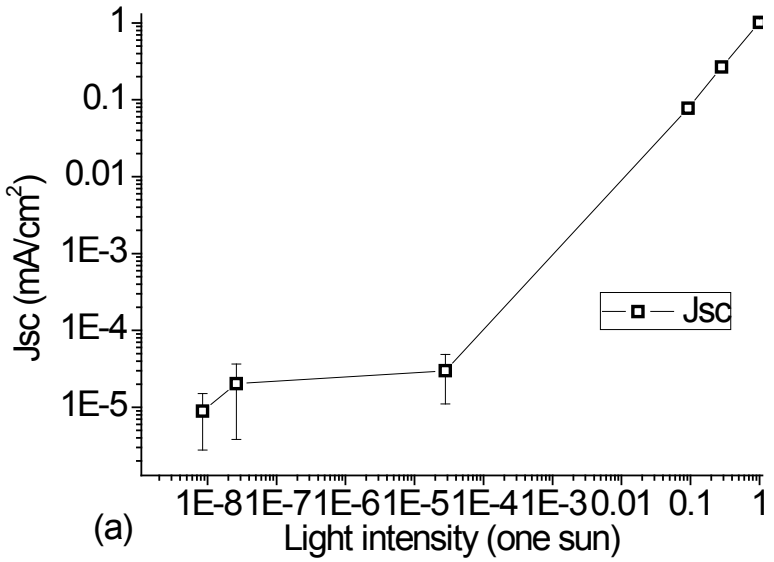

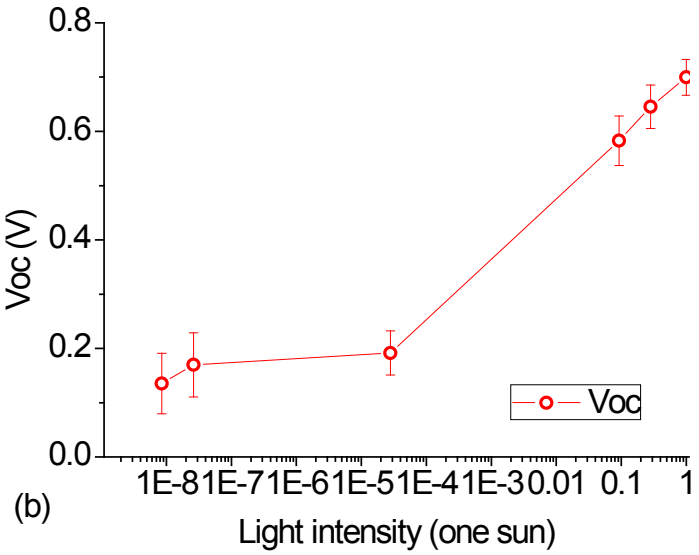

Fig. 7-5 The measured output signal of 10 μm in response to low light intensity (a) Jsc; (b) Voc.

7.4 SCAPS feedback based on measurement

In order to better understand the device performance, and to more accurately simulate its output under diagnostic X-ray beams, some parameters in the SCAPS software should be adjusted and tested.

One important parameter used in the SCAPS that we can tune is the density of defect, N_d, in CdTe layer. N_d is a quality indicator of the material. The commonly accepted value in the solar cell baseline model is 2×10^{14} cm^{-3}. Shown in Fig. 7-6 is the change in the output signal of 3 μm thick device for 80 kVp after we manipulate the defect density value, both below and above the baseline value. As we can see, the open circuit voltage (Voc) decreases with the defect density, while Jsc is almost independent on this parameter.

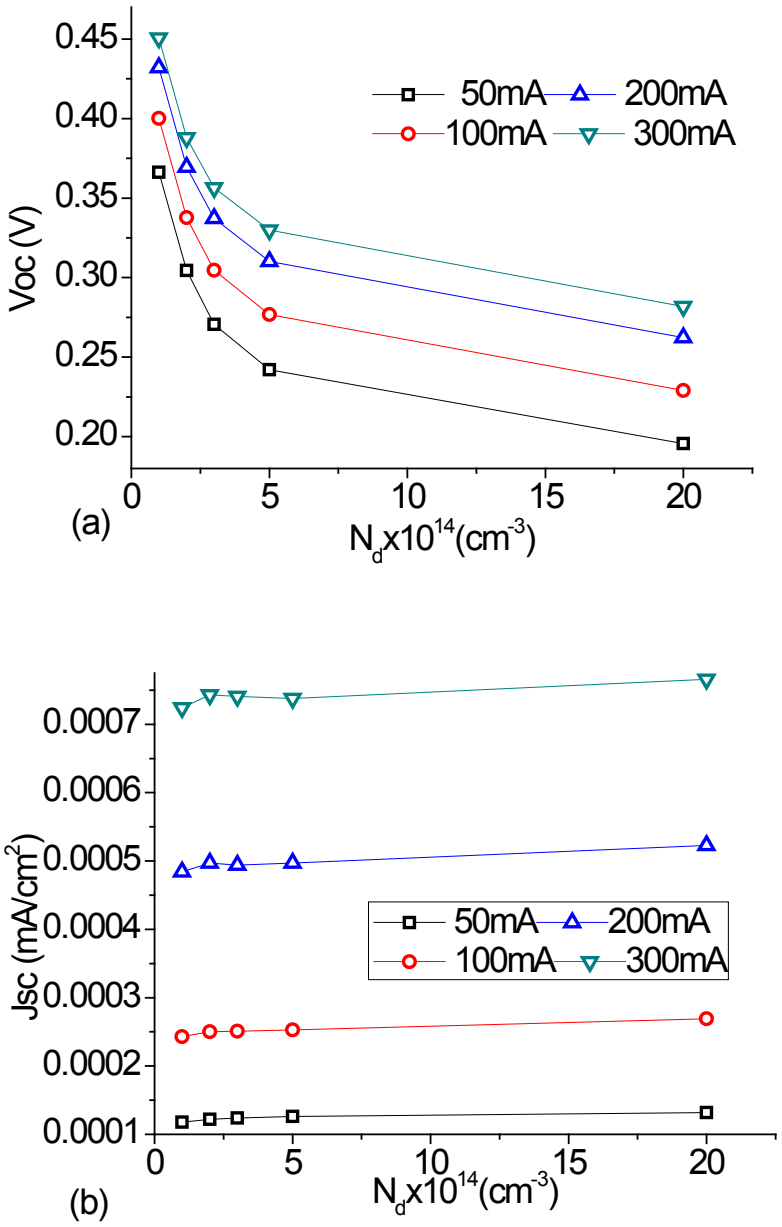

Fig. 7-6 The changes of output signal of 3 μm CdTe layer for 80 kVp as a function of defect density (a) Voc; (b) Jsc.

Measurement verifications and careful self-consistent manipulation of material parameters enable modeling of the device performance more accurately with SCAPS. Shown in Fig. 7-7 is an example of simulated and measured I-V curves with matched short-circuit currents.

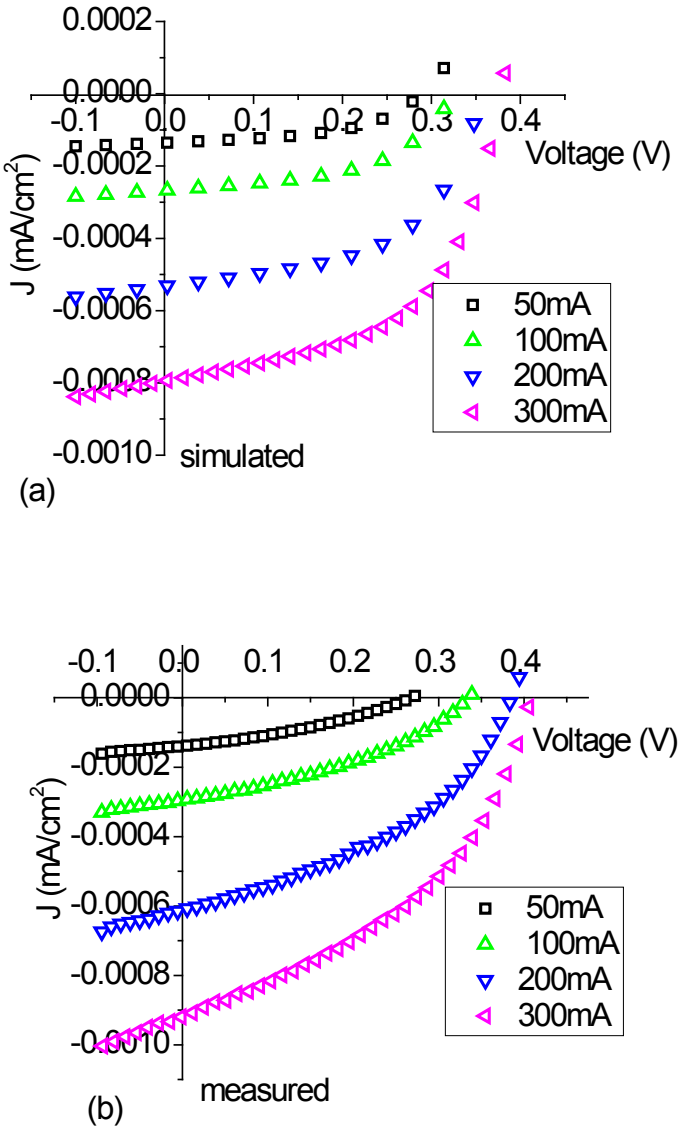

Fig. 7-7 I-V curves for one 10 μm thick detector under 120 kVp beam: (a) simulated; (b) measured.

7.5 Time response study

The time required for a detector output to go from the initial value to a percentage (e.g. 90%) of the final value is called the response time. The rise time is the time required for the detector to fully respond to the incoming X-ray beam; it is typically

defined as the interval between the times at which the signal reaches 10% and 90% of the final value. Similarly, the fall time is the time required for the detector output to diminish to the background value after the beam is turned off, again defined as the interval between the times at which the output signal falls from 90% to 10% of the initial value.

The response of CdTe detectors to the diagnostic X-ray beams generated by Varian Ximatron Simulator were recorded with a digital Tektronix oscilloscope (model 200). The measurement setup is similar to that of the I-V curve measurement. Samples were wrapped in black cloth, and open-circuit voltage signals were collected and recorded by the digital oscilloscope relying on the built-in electric field.

The time response characteristics of CdTe to diagnostic X-ray beams were analyzed by exponential fitting on the obtained step response curves. Shown in Fig. 7-8 and Fig. 7-9 are the rise time and fall time analysis examples, respectively. The average rise time and fall time for these CdTe detectors with the diagnostic X-ray beams are each around 5 ms.

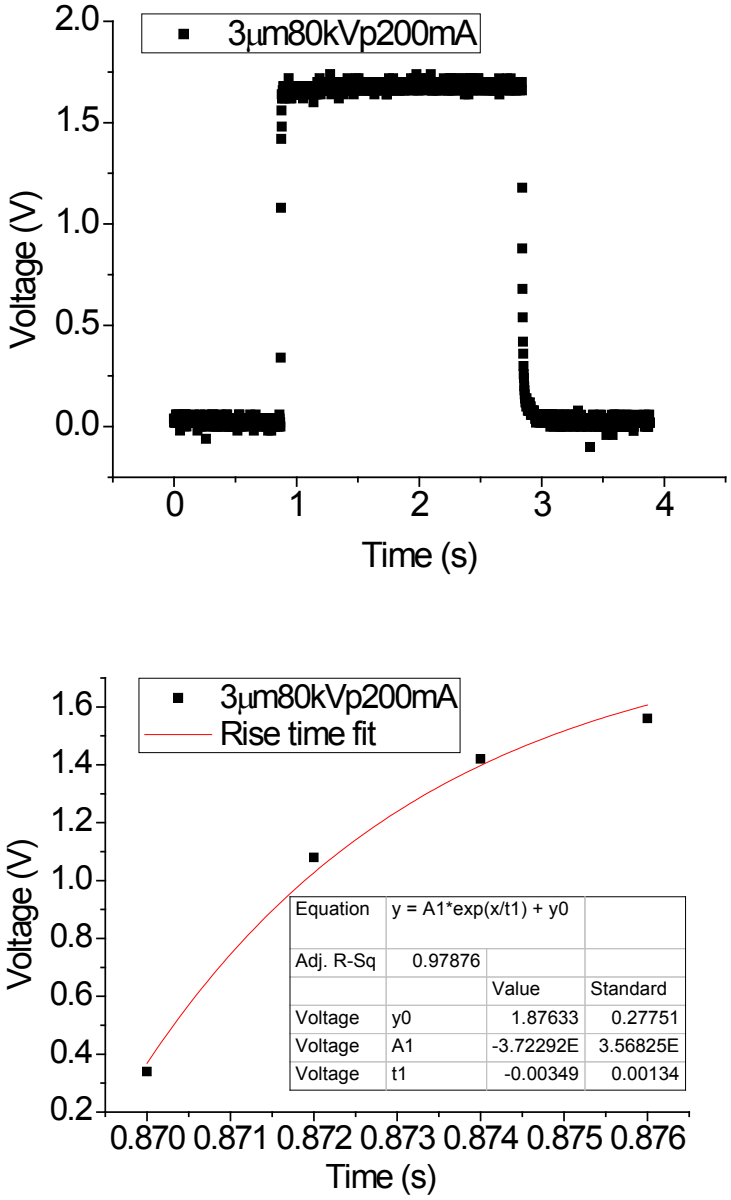

Fig. 7-8 Measured open circuit voltage of 3 μm thin film CdTe for 80 kVp 200 mA beam: (a) typical step response signal time dependence; (b) rise time analysis and its fit curve.

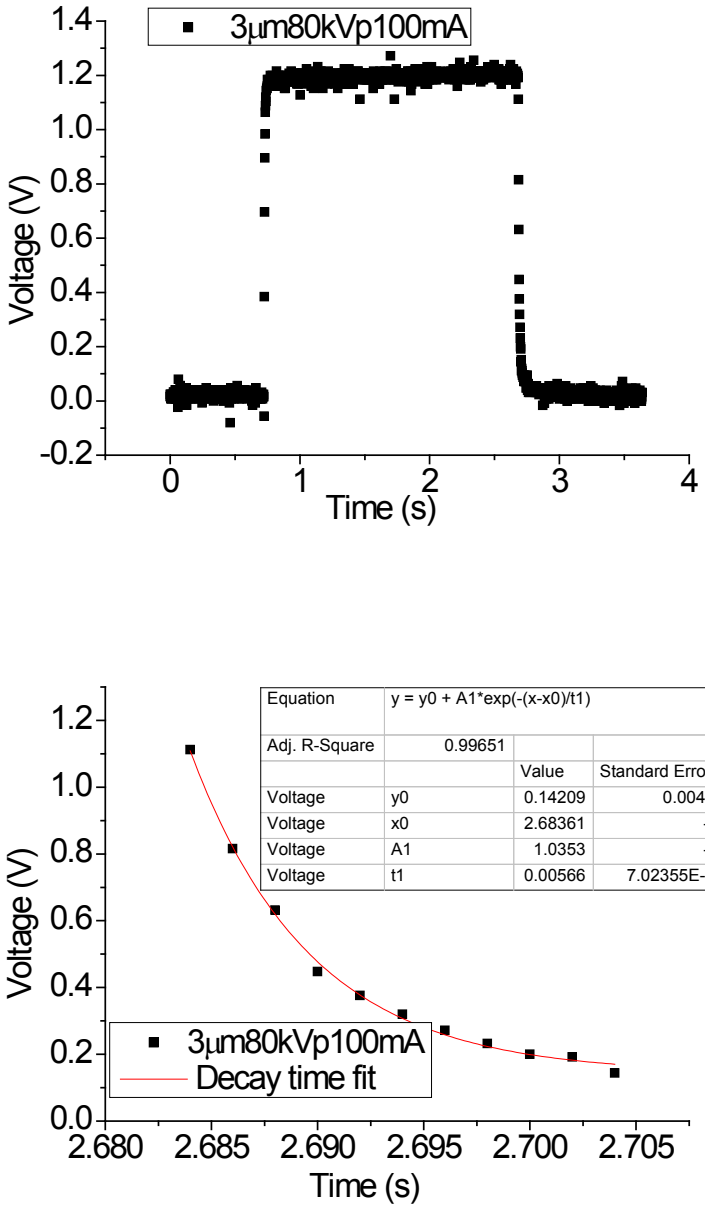

Fig. 7-9 Measured open circuit voltage of 3 μm thin film CdTe for 80 kVp 100 mA beam: (a) typical step response signal time dependence; (b) fall time analysis and its exponential fit curve.

In general, the response time is controlled by the charge carrier dynamics, such as the mobility, lifetime, applied bias, and recombination ratio, etc. The response times of 5 ms of our measurement are not improved very much compared with early studies.[108] However, according to continuity equation and Ramo's theory,[109] we can estimate the temporal response of the detector from:

$$t = \frac{L}{\mu E} \qquad (7\text{-}1)$$

where L is the detector thickness, μ is the mobility of a charged particle, and E is the applied electric field. For 3 μm CdTe, based on its electron mobility around 10^3 $cm^2/V/s$, and with a built-in potential of 10^4 V/cm, the response time for an ideal polycrystalline CdTe detector is around 10 ps. Actually, a time response of 5 ns has been reported for a polycrystalline CdTe detector with a thickness of 300 μm under a laser pulse (35 ps FWHM, 1066 nm wavelength).[110] Our measurement results most probably reflect the shape of the trailing edge of the X-ray beam pulse itself.

Chapter 8

Conclusion

This Dissertation evaluated the thin film polycrystalline CdTe material as a direct radiation detector for large area digital diagnostic X-ray imaging application. We found that a thin film polycrystalline CdTe detector is very promising for large area diagnostic X-ray imaging.

The diagnostic X-ray spectra needed for the detector investigation were first calculated by using the tungsten anode spectral model using interpolating polynomials (TASMIP) technique. The diagnostic X-ray spectra from 70 kVp to 140 kVp of our Varian simulator with tungsten target were accurately calculated by using published measured Fewell spectra and measured simulator output. Primary photons spectra obtained a 20 cm water phantom were used as input in Monte Carlo simulations of imaging properties of CdTe detector.

The following trends in behavior of intrinsic imaging parameters were established. The spatial resolution characteristic, MTF, decreases with the detector thickness and the tube potential. The noise power spectrum, NPS, increases with the detector thickness and the tube potential. Detective quantum efficiency, DQE, increases with the detector thickness, gradually saturating for thickness above 600 μ m. Optimal thickness of thin film CdTe detector for diagnostic X-ray imaging application is between 300 μm and 600 μm. Comparison with other detector materials indicates that a-Se has a better spatial resolution than CdTe and HgI_2, while CdTe shows DQE

superior to those of a-Se and HgI_2 under diagnostic X-ray beams, especially at higher kVp values.

Energy deposition across the thin film CdTe detector was investigated by Monte Carlo simulation with MCNP5, and charged carriers profiles (electron-hole pairs) were calculated and employed as input into the SCAPS device operation simulations. An electronic characteristics study with SCAPS indicates the output current is linear with deposited energy, and the output voltage is in a logarithmic relationship with deposited energy. The output signal increases with the detector thickness, but reaching saturation after 300 μm.

A device performance study with the measurements indicates that a thin film CdTe detector has adequate sensitivity and linearity for its application for diagnostic X-ray beams. Comparison between measured output signals and SCAPS simulation results implies that there is room for improvement in the SCAPS model by self-consistent parameter adjustments.

Overall, we conclude that thin film polycrystalline CdTe detector is very promising for large area digital imaging application under diagnostic X-ray beams, and has a high potential of being implemented in a commercial direct detection AMFPI system.

References

[1] Antonuk L E, "Electronic portal imaging devices: a review and historical perspective of contemporary technologies and research," Phys. Med. Biol., 2002, 47, R31-65.

[2] Antonuk L E, "a-Si:H TFT based active matrix flat-panel imagers for medical X-ray applications," Thin Film Transistors, Materials and Processes Vol 1: Amorphous Silicon Thin Film Transistors vol 1, ed Y Kuo (Boston Kluwer), p p 395-484, 2004.

[3].Street R A (ed) "Technology and application of amorphous silicon," Vol 37 (Berlin: Springer), 2000.

[4] L. E. Antonuk, J. Yorkston, W. huang, J. H. Sieverdsen, J. M. Boudry, Y. El-Mobri, and M. V. Marx, "A real-time, flat-panel, amorphous silicon, digital X-ray imager," RadioGraphics, 1995, 15, 993-1000.

[5] J. A. Rowlands, W. Zhao, I. M. Belvis, D. F. Waechter, and Z. Huang, "Flat-panel digital radiology with amorphous selenium and active-matrix readout," Radiographics, 1997, 17, 753-760.

[6] J. A. Rowlands, and J. Yorkston, "Flat panel detectors for digital radiography," in Handbook of Medical Imaging Volume I: Physics and Psychophysics (ed. J. Bcutel, H. L. Kundel, and R. L. van Metter) SPIE Press, Bellingham, WA, 2000

[7] Granfors P R, Albagli D, Tkaczyk E J, Aufrichtig R, Netel H, Brunst G, Boudry J, and Luo D, "Performance of a flat panel cardiac detector," Proc, SPIE 2001, 4320, 77-86.

[8] R. E. Colbeth, S. J. Boyce, R. Fong, K. W. Gray, R. A. Harris, I. D. Job, I. P. Mollov, B. Nepo, J. M. Pavkovich, N. Taie-Nobaries, E. J. Seppi, E. G. Shapiro, M. D. Wright, C. Webb, and J. M. Yu, "40*30 cm^2 flat panel imager for angiography, R&F, and cone-beam CT application," Proc. SPIE, 2001, 4320, 94-102.

[9] Ikeda S, Suzuki K, Ishikawa K, Colbeth R E, Webb C, Tanaka S and Okusako K, "Development and evaluation of a digital radiography system using a large-area flat panel detector," Proc. SPIE, 2001, 5030, 215-25.

[10] Samei E AND Flynn M J, "An experimental comparison of detector performance for direct and indirect radiography systems," Med. Phys., 2003, 30 608-22.

[11] S. Vedantham, A. Karellas, S. Suryanarayanan, I. Levis, and C. J, D'Orsi, "Full breast digital mammography with an amorphous silicon-based flat panel detector: physical characteristics of a clinical prototype," Med. Phys., 2000, 27(3), 558-67.

[12] Zhao B and Zhao W, "Characterization of a direct, full-field flat panel digital mammography detector," Proc. SPIE, 2003, 5030, 157-67.

[13] Tousignant O, Demers Y, Laperriere L, Nishiki M, Nagai S, Tomisaki T, Takahashi A and Aoki K, "Clinical performances of a 14'' * 14'' real time amorphous selenium flat panel detector," Proc.SPIE, 2003, 5030, 71-6.

[14] W. Zhao, J.A. Rowlands, "Digital radiology using active matrix readout of amorphous selenium: Theoretical analysis of detective quantum efficiency," Med. Phys., 1997, **24**, 1819-1833.

[15] W. Zhao, I. Blevis, S. Germann, J.A. Rowlands, D. Waechtcher, and Z.S. Huang, "Digital radiography using active matrix readout of amorphous selenium: construction and evaluation of a prototype real-time detector," Med. Phys., 1997, **24**, 1834-1843.

[16] D.L. Lee, L.K. Cheung, B.G. Rodricks, G.F. Powell, "Improved imaging

performance of a 14×17-inch direct radiography™ system using Se/TFT detector," Proc. SPIE, 1998, **3336**, 14-23.

[17] A. Tsukamoto, S. Yamada, T. Tomisaki, M. Tanaka, T. Sakaguchi, K. Suzuki, and M. Ikeda, "Development and evaluation of a large-area Selenium-based flat-panel detector for real-time radiography and fluoroscopy," Proc. SPIE, 1999, **3659**, 14-23.

[18] L. E. Antonuk, K.-W. Jee, Y. El-Mohri, M. Maolinbay, S. Nassif, X. Rong, Q. Zhao, J. H. Siewerdsen, R. A. Street, K. S. Shah, "Strategies to improve the signal and noise performance of active matrix, flat-panel imagers for diagnostic X-ray applications," Med. Phys., 2000, **27**, 289-306.

[19] H. Du, L. E. Antonuk, Y. El-Mohri, Q. Zhao, Z. Su, J. Yamamoto, and Y. Wang, "Signal behavior of polycrystalline HgI_2 at diagnostic energies of prototype, direct detection, active matrix, flat-panel imagers," Phys. Med. Biol., 2008, 53, 1325-1351.

[20] G. Zentai, L. Partain, R. Pavlyuchkova, G. Virshup, A. Zuck, L. Melekhov, O. Dagan, A. Vilensky, H. Gilboa, "Large area Mercuric Iodide X-ray imager," Proc. SPIE, 2002, **4682**, 592-600.

[21] Z. Su, L. E Antonuk, Y. El-Mohri, L. Hu, Hong Du, Amit Sawant, Y. Li, Y. Wang, J. Yamamoto and Q. Zhao, "Systematic investigation of the signal properties of polycrystalline HgI_2 detectors under mammographic, radiographic, fluoroscopic and radiotherapy irradiation conditions," Phys. Med. Biol., 2005, **50,** 2907–2928.

[22] K.S. Shan, P.R. Bennett, M. Klugerman, L.P. Moy, G. Entine, D.R. Ouimette, and R. Aikens, "Lead iodide films for X-ray imaging," P roc. SPIE, 1997, **3032**, 395-404.

[23] R.A. Streat, J.T. Rahn, S.E. Ready, K.S. Shah, P.R. Bennett, Y.N. Dmitriyev, P. Mei, J.P. Lu, R.B. Apte, J. Ho, K. Van Schuylenbergh, F. Lemmi, J.B. Boyce, and

P.Nylen, “X-ray imaging using lead iodide as a semiconductor detector, ” Proc. SPIE, 1999, **3659**, 36-47.

[24] Y. Kang, L. E. Antonuk, Y. El-Mohri, L. Hu, Y. Li, A. Sawant, Z. Su, Y. Wang, J. Yamamoto , and Q. Zhao, “Examination of PbI_2 and HgI_2 photoconductive materials for direct detection, active matrix, flat-panel imagers for diagnostic X-ray imaging,” IEEE Trans. Nucl. Sci., 2005, **52**, 38-45.

[25] M. Simon, R. A. Ford, A. R. Franklin, S. P. Grabowski, B. Menser, G. Much, A. Nascetti, M. Overdick, M. J. Powell, and D. U. Wiechert, “PbO as direct conversion X-ray detector material,” Proc. SPIE, 2004, **5368**, 188-199.

[26] D.R. Ouimette, S. Nudelman, and R.S. Aikens, “A new large-area X-ray image sensor,” Proc. SPIE, 1998, **3336**, 470-476.

[27] S. Adachi, N.Hori, K. Sato, K. Uehara, Y. Izumi, H. Nagata, Y. Yoshimura, S. Yamada, “Experimental evaluation of a-Se and CdTe flat-panel X-ray detectors for digital radiography and fluoroscopy,” Proc. SPIE, 2000, **3977**, 38-47.

[28] S. Tokuda, S. Adachi, T. Sato, T. Yoshimuta, H. Nagata, K. Uehara, Y. Izumi, O. Teranuma, S. Yamada, “Experimental evaluation of a novel CdZnTe flat-panel X-ray detector for digital radiography and fluoroscopy,” Proc. SPIE, 2001, **4320**, 140-147.

[29] S. Tokuda, H. Kishihara, S. Adachi, T. Sato, Y. Izumi, O. Teranuma, Y. Yamane, S. Yamada, “Large-area deposition of a polycrystalline CdZnTe film and its applicability to X-ray panel detectors with superior sensitivity,**”** Proc. SPIE, 2002, **4682**, 30-41.

[30] S. Tokuda, H. Kishihara, S. Adachi, T. Sato, “Improvement of the temporal response and output uniformity of polycrystalline CdZnTe films for high sensitivity X-ray imaging,” Proc. SPIE, 2003, **5030**, 861-870.

[31] C. Choi, C. Kyun, S. Kang, and S. Nam, “Comparison of compound

semiconductor radiation films deposited by s creen printing method," Proc. SPIE, 2007, **6510**, 421-8.

[32] M. Hoheisel, J. Giersch, P. Bernhardt, "Intrinsic spatial resolution of semiconductor X-ray detectors: a simulation study," Nucl. Instr. and Meth. A, 2004, 531, 75-81.

[33] W. Akuagawa, K. Zanio, and J. W. Mayer, "CdTe as a gamma detector," Nucl. Instrum. Methods, 1967, 55, 383-385.

[34] Y. Eisen, and E. Polak, "An array of CdTe detectors for imaging applications," Mat. Res. Soc. Symp. Proc., 1993, 302, 487.

[35] H. B. Barber, B. A. Apotovsky, F. L. Augustine, H. H. Barrett, E. L. Dereniak, F. P. Doty, J. D. Eskin, W. J. Hamilton, D. G. Marks, K. J. Matherson, J. E. Venzon, J. M. Woolfenden, and E. T. Young, "Semiconductor pixel detectors for gamma-ray imaging in nuclear medicine," Nuclear Instruments and methods in physics research section A, 1997, 395, 421-428.

[36] A. Niemela, and H. Sipila, "Evaluation of CdZnTe detector for soft X-ray applications," IEEE Transaction on Nuclear Science, 1994, 361, NS-41.

[37] A. Parsons, C.M. Lisse, C.M. Stahle, N. Gehrels, B. J. Teegarden, S. Babu, N. Cao and P. Shu, "Room temperature CdZnTe detectors for hard X-ray astrophysics," IEEE Transactions on Nuclear Science, 1994, 2, 781.

[38] Y. Eisen, "Current state-of-the-art applications utilizing CdTe detectors," Nuclear Instruments and Methods A, 1992, 322, 596-603.

[39] R. Arlt, K.H. Czock, and D.E Rundquist, "Overview of the. use of CdTe Detectors for the Verification of Nuclear Material in Nuclear Safeguards," Nuclear Instruments and Methods A, 1992, 322, 575.

[40] F . G lasser, G. Thomas, M. Cuzin, and L. Verger, "Application of cadmium

telluride detectors to high energy computed tomography," Nuclear Instruments and Methods in Physics Research, 1992, A322, 619-622.

[41] M. Hage-Ali, and P. Siffert, "Growth methods of CdTe nuclear detector materials," In Semiconductors for Room Temperature Nuclear Detector Application, Eds. T. E. Schlesigner, R. B. James, Academic Press, San Diego, CA, USA, 43, 219-257, 1995.

[42] J. F. Butler, "Novel electrode design for single-carrier charge collection in semiconductor nuclear radiation detectors," Nuclear Instruments and Methods, 1997, A396, 427-430.

[43] H. L. Malm, and M. Martini, "Polarization phenomena in CdTe nuclear detectors," IEEE Trans. Nucl. Sci., 1974, 21, 322-330.

[44] C. Ferekides, J. Britt, Y. Ma, and L. Killian, "High Efficiency CdTe Solar Cells by Close Spaced Sublimation," Proceedings of 23rd Photovoltaic-Specialist Conference IEEE, NY, p.389 1993.

[45] A. Bosio, N. Romeo, S. Mazzamuto, and V. Canevari, "Polycrystalline CdTe thin films for photovoltaic applications," Progress in Crystal Growth and Characterization of Materials, 2006, 52, 247-279.

[46] NIST database http://www.nist.gov/pml/data/xcom/index.cfm

[47] Diana Shvydka, E.I. Parsai, and J. Kang, "Radiation hardness study of CdTe thin films for use in high-energy photon beam detectors," Nucl. Instrum. Meth. A, 2008, **586**, 169-173.

[48] A. Cavallini, B. Fraboni, W. Dusi, N. Auricchio, P. Chirco, M. Zanarini, P. Siffert, P. Fougeres, "Radiation effects on II–VI compound-based detectors", Nucl. Instr. And Meth. A, 2002, 476, 770-778.

[49] Y. Eisen, L.G. Evans, S. Floyd, C. Schlemm, R. Starr, J. Trombka, "Radiation damage of Schottky CdTe detectors irradiated by 200 M eV protons," Nucl. Instr. And Meth. A, 2002, 491, 176-180.

[50] D.L. Batzner, A. Romeo, M. Dobeli, K. Weinert, H. Zogg, A.N. Tiwari, "High energy irradiation properties of CdTe/CdS solar cells," IEEE Proceedings, p. 982-985, 2002.

[51] E. Rossa, H. Schmickler, A. Brambilla, L. Verger, F. Mongellaz, "New development of a radiation--hard polycrystalline CdTe detector for LHC luminosity monitoring," DIPAC 2001 Proceedings - ESRF, Grenoble, 2001.

[52] M. Hoheisel, J. Giersch, and P. Bernhardt, "Intrinsic spatial resolution of semiconductor X-ray detectors: a simulation study," Nuclear Instruments & Methods In Physics Research A, 2004, 531, 75-81.

[53] J. M. Boone and J. A. Seibert, ''An accurate method for computer generating tungsten anode X-ray spectra from 30 to 140 kV,'' Med. Phys. 1997, **24**, 1661–1670.

[54] M. M. Blough, R. G. Waggener, W. H. Payne, and J. A. Terry, "Calculated mammographic spectra confirmed with attenuation curves for molybdenum, rhodium, and tungsten targets," Med. Phys., 1998, 25, 304-310.

[55] M. R. Ay, M. Shahriari, S. Sarka, M. Adib, and H. Zaidi, "Monte Carlo simulation of X-ray spectra in diagnostic radiology and mammography using MCNP4C," Physics in Medicine and Biology, 2004, 49, 4897-4917.

[56] T.R. Fewell and R.E. Shuping, and K.E. Healy, Handbook of Computed Tomography X-ray Spectra, HHS Publication (FDA) 81-8162 (U.S. Government Printing Office, Washington, D.C., 1981).

[57] F. B. Brown, MCNP - A General Monte Carlo N-Particle Transport Code, Version

5, LA-UR-03-1987, Los Alamos National Laboratory 2003.

[58] W. Swindell, E. J. Morton, P. M. Evans, and D. G. Lewis, "the design of megavoltage projection imaging systems: some theoretical aspects," Med. Phys., 1991, 18, 855-866.

[59] D. W. O. Rogers, "Low energy electron transport with EGS," Nucl. Instrum. Methods, 1984, 227, 535-548.

[60] A. F. Bielajew and D. W. O. Rogers, in Monte Carlo Transport of Electrons and Photons, edited by T. M. Jenkins, W. R. Nelson, A. Rindi, A. E. Nahum, and D. W. O. Rogers (Prenum, New York, 1988), pp. 115-137.

[61] H. E. Johns, and J. R. Cunningham, The physics of Radiology, Thomas, Springfield, 1983.

[62] F. H. Attix, Introduction to Radiological Physics and Radiation Dosimetry, Wiley, New York, 1986.

[63] G. Hajdok, J. J. Battista, and I. A. Cunningham, "Fundamental limitations imposed by X-ray interactions on the modulation transfer function of existing X-ray detectors," Proceedings of SPIE, 2003, 5030, 1-15.

[64] M. Hoheisel, J. Giersch, M. Mitschke, and P. Bernhardt, "Absorbers for medical X-ray detector with optimum spatial resolution: a simulation study," Proceedings of SPIE, 2004, 5368, 386-395.

[65] H. Fujita, D. Y. Tsai, T. Itoh, K. Doi, J. Morishita, K. Ueda, and A. Ohtsuk, "A simple method for determining the modulation transfer-function in digital radiography," IEEE Trans. Med. Phys., 1997, **24**, 51-70.

[66] D.L. Lee, L.K. Cheung, E.F. Palechi, and L.S. Jeromin, "A discussion on resolution and dynamic range of Se-TFT direct digital radiographic detector," Proc.

SPIE, 1996, **2708,** 511-522.

[67] J.M. Boone, J.A. Seibert, J.M. Sabol, and M. Tecotzky, "A Monte Carlo study of X-ray fluorescence in X-ray detectors," Med. Phys., 1999, **26**, 905-916.

[68] A. Rose, "A unified approach to the performance of photographic film, television pick-up tubes and the human eyes," J. Soc. Motion Pict. Eng., 1946, 47, 273-294.

[69] A. Rose, "The sensitivity performance of the human eye on an absolute scale," J. Opt. Soc. Am., 1984, 38, 196-208.

[70] A. Rose, "Quantum and noise limitations of the visual process," J. Opt Soc. Am., 1953, 43, 715-716.

[71] I. A. Cunningham and R Shaw, "Signal-to-noise optimization of medical imaging systems," J. Opt. Soc. Am. A, 1999, 16, 621-632.

[72] A. E. Burgess, "The Rose model, revisited," J. Opt. Soc. Am. A, 1999, 16, 633-646.

[73] R. Shaw, "The equivalent quantum efficiency of the photographic process," J. Photogr. Sci., 1963, 11, 199-204.

[74] J. C. Dainty and R. Shaw, Image Science (Academic, New York, 1974)

[75] C. E. Metz, and C. J. Vyborny, "Wiener spectral effects of spatial correlation between the sites of characteristic X-ray emission and reabsorption in radiographic screen-film systems," Phys. Med. Biol., 1983, 28, 547-564.

[76] J.C.Dainty and R. Shaw, Imaging Science: Principles, Analysis and Evaluation of Photographic-Type Imaging Processes (Academic, London, 1974).

[77] J. T. Dobbins, D. L. Ergun, L. Rutz, D. A. Hinshaw, H. Blume, and D.C. Clark, "DQE (f) of four generations of computed radiography acquisition devices," Med Phys., 1995, 22,1581-1593.

[78] J.H. Siewerdsen, L.E. Antonuk, Y. EI-Mohri, J. Yorkston, W. Huang, and I.A. Cunningham, "Signal, noise power spectrum, and detective quantum efficiency of indirect-detection flat-panel imagers for diagnostic radiology," Med. Phys., 1998, **25**, 614-628.

[79] H. P. Chan, and K. Doi, "Studies of X-ray energy absorption and quantum noise properties of X-ray screens by use of Monte Carlo simulation," Med. Phys., 1984, 11, 37-46.

[80] G. Hajdok, J. Yao, J. J. Battista, and I. A. Cunningham, "Signal and noise transfer properties of photoelectric interactions in diagnostic X-ray imaging detectors," Med. Phys., 2006, 33, 3601-3620.

[81] D. A. Jaffray, J. J. Battista, A. Fenster, and P. Munro, "Monte Carlo studies of X-ray energy absorption and quantum noise in megavoltage transmission radiography," Med. Phys., 1995, **22**, 1077-1088.

[82] I. Cunningham, "Applied linear-systems theory," in Handbook of Medical Imaging, edited by J.Beutel, H.L. Kundel, and R.L. Van Metter (SPIE Press, Bellingham, Washington, 2000), pp. 79-159.

[83] R. K. Swank, "Absorption and noise in X-ray phosphors," J. Appl. Phys., 1973, 44, 4199-4201.

[84] M.J. Yaffe, R.M. Nishikawa, "X-ray imaging concepts: Noise, SNR and DQE," in Specification, Acceptance Testing and Quality Control of Diagnostic X-ray Imaging Equipment, Medical Physics Monograph No.20, Edited by J. A. Seibert, G.T. Barnes, R.G. Gould, p. 109-144 (AIP, New York, 1994).

[85]A. L. Fahrenbruch and R. H. Bube, "Fundamentals of Solar Cells," (Academic, New York, 1983).

[86]H. J. Leany, L. C. Kimerling, and S. D. Ferris, "Electron beam induced current," Scanning electron Microscopy, 1978, **1**, p71.

[87] R. Harju, V. G. Karpov, D. Grecu, and G. Dorer, "Electron-beam induced degradation in CdTe photovoltaics," J. Appl. Phys., 2000, **88**, 1794-1801.

[88] D. S. McGregor and H. Hermon, "Room-temperature compound semiconductor radiation detectors," Nucl. Instrum. Meth. A, 1997, 395, 101-124.

[89] G. F. Knoll, "Radiation detection and measurement," 3d edition, p.115 (Hoboken, NJ: Wiley, 2000).

[90] M. Burgelman, P. Nollet, and S. Degrave, "Modeling polycrystalline semiconductor solar cells," Thin Solid Films, 2000, 361 -362, 527-532. also see Http://trappist.elis.ugent.be/ELISgroups/solar/projects/scaps.html

[91]A. Niemegeers, M. Burgelman, "Numerical modeling of ac-characteristics of CdTe and CIS solar cells," Conference Record, 25th IEEE Photovoltaic Specialists Conference, Washington DC, April 1996, 901–904.

[92] A. Owens and A. Peacock, " Compound semiconductor radiation detectors," Nucl. Instrum. Methods Phys. Res. A, 2004, **531**(2), 18

[93] M. Burgelman, P. Nollet, S. Degrave, "Modeling Polycrystalline Semiconductor Solar Cells," Thin Solid Films, 2000, 361, 527-532.

[94] Developed by M. Gloeckler, now part of the SCAPS distribution package.

[95] H. Nishizawa, H. Inujima, and K. Takashima, "Improvement of the spectral response in large CdTe detectors operating at low bias voltage," IEEE transactions on nuclear science, 2002, 49, 2025-2031.

[96] D. Shvydka, V. G. Karpov, and A. D. Compaan, "Bias-dependent Photoluminescence in CdTe photovoltaics," Appl. Phys. Lett., 2002, **80**, 3114-3116.

[97] S. M. Sze, Physics of Semiconductor Devices. John Willey &Sons, New York, 1981.

[98] M. Burgelman, J. Verschraegen, S. Degrave, and P. Nollet, "Modeling thin-film PV devices," Prog. Photovolt: Res. Appl, 2003, 11, 1-11.

[99] H. Pauwels, G. Vanhoutte, "The influence of interface states and energy barriers on the efficiency of heterojunction solar cells," Journal of Physics D: Applied Physics, 1978, 11, 649-667.

[100] R. B. James, P. Siffert, Eds 11th Interantional Workshop on Room Temperature Semiconductors and Associated Electronics. Nucl. Instrum. Methods Phys. Res. A, 2001, 458: 1-603.

[101] B. Philps, Ed. 15th International Workshop on Room-Temperature Semiconductor X- and Gamma-Ray Detectors. IEEE Nucl. Sci. Symp. Conf. Rec., 2006, 6, 3585-3939.

[102] T. L. Chu, S. S. Chu, F. Firszt, H.A. Naseem, and R. Stawski, "Deposition and characterization of ***p*** - type cadmium telluride films," J. Appl. Phys., 1985, 58, 1349-1356.

[103] J. Barker, S. P. Binns, D. R. Johnson, R. J. Marshall, S. Oktik, M. E. Oznan, M. H. Patterson, S. J. Ransome, .S. Roberts, M. Sadeghi, J. M. Sherborne, A. K. Turner, and J. M. Woodcock, "Electrodeposited CdTe for thin film solar cells," International journal of solar energy, 1992, 12, p25.

[104] T. L. Chu, S. S. Chu, C.Ferekides, C. Q. Wu, J. Britt, C. Wang, "13.4% efficient thin - film CdS/CdTe solar cells," Journal of Applied Physics, 1991, **70**7, p608.

[105] C. S. Ferekides, D. Marinskiy, V. Viswanathan, B, Tetali, V. Palekis, P. Salvaraj, and D. L. Morel, "High Efficiency CSS CdTe Solar Cells," *Thin Solid Films,* 2000,

361-362,.p520-526.

[106] D. Shvydka, V. G. Karpov, and A. D. Compaan, “Low Light Divergence In Photovoltaic Parameter Fluctuations,” *Appl. Phys. Lett.2003,* **82**, 2157-2159.

[107] S. Adachi, N. Hori, K. Sato, S. Tokuda, T. Sato, K. Uehara, Y. Izumi, H. Nagata, Y. Yoshimur, and S. Yamada, “Experimental evaluation of a-Se and CdTe Flat-Panel X-ray detectors for digital radiography and fluoroscopy,” Proceedings of SPIE, 2000, 3977, 38-47.

[108] W. C. Barber, E. Nygard, J. C. Wessel, N. Malakhov, G. Wawrzyniak, N. E. Hartsough, T. Gandhi, and J. S. Iwanczyk, “Fast photon counting CdTe detectors for diagnostic clinical CT: dynamic range, stability, and temporal response,” Proc. of SPIE, 2010, 7622, 76221E-1-8.

[109] F. Mathy, A. Gliere, E. G. d’Aillon, P. Masse, M. Picone, J. Tabary, and L. Verger, “A three-dimensional model of CdZnTe gamma-ray detector and its experimental validation,” IEEE Trans. Nucl. Sci., 2004, 51, 2419-26.

[110] E. Rossa, H. Schmickler, A. Brambilla, L. Verger, and F. Mongellaz, “New development of a radiation-hard polycrystalline CdTe detector for LHC luminosity monitoring, ” Proceedings DIPAC 2001- ESRF, Grenoble, France.

Appendix A

The Polynomial Fit Coefficients for Spectra Calculation

a0	a1	a2	a3
-0.0000127001987858816	0.00417969090547376	-0.461559939612097	17.4306009744154
0.0001101242815589830	-0.02848761609934490	2.331897754908940	-56.0682876521972
0.0004285319223020380	-0.11277167936056900	9.597913292479250	-251.7212710734110
0.0002990814337010370	-0.05514595380852380	2.230355139517480	66.1458607587756
-0.0001516273345682690	0.10161999321815700	-14.952716843591400	722.9802535305710
-0.0004151208618364120	0.23422748433666200	-32.629566238806500	1590.0644771821400
-0.0007848543131885150	0.39623202554512400	-52.439188563837400	2565.4635179558300
-0.0022603720915757900	0.92618705628859600	-108.861875224682000	4958.5184873053700
-0.0042485075768256600	1.58838854301498000	-174.434395048094000	7627.4063199932500
-0.0026926618807497000	1.11938962825533000	-122.274365979308000	6201.6816971467100
-0.0007720283072941330	0.52162731890416600	-54.780966427307100	4231.5428398642500
-0.0032027731618944200	1.23314870595762000	-114.026066755474000	6278.2559395899100
-0.0060354844529736000	2.05108925505537000	-181.429688043848000	8537.7842961129400
-0.0038850132333131300	1.37816321503161000	-98.852674366674300	5816.8063430431500
-0.0016042080262915800	0.66504767395499600	-11.749054384685900	2918.4378864309000
-0.0038797257392439200	1.37186582755412000	-69.525948197008500	4723.9089331790300
-0.0064095578478174800	2.15829942516872000	-135.020950256630000	6764.0396603973300
-0.0045857803061302600	1.53081748721083000	-53.525298009810200	3763.8067122105500
-0.0027211000237251000	0.88573158637753800	30.602028043070900	650.4720280171080
-0.0043307462522917200	1.39148720507929000	-8.423673684677000	1591.8136577844700
-0.0061035887064303400	1.94640943837991000	-51.845474783504900	2656.4467415020100
-0.0039735624270005700	1.34253835287748000	12.294806714351200	427.5615341583980
-0.0018500592593632300	0.74152061178103800	76.298909322415500	-1804.0037491609300
-0.0048419271156879300	1.69056419077860000	-13.400640272123600	851.6081857608060
-0.0079311870635809500	2.67102937999441000	-106.277760238668000	3606.9554429885200
-0.0063117518699383100	2.20672982126527000	-58.168220258036900	1855.2320953369600
-0.0046466729789990900	1.73177443905240000	-9.440557548522090	90.3192084200268
-0.0053303017135932900	1.97418993964820000	-34.054098446750000	755.4972754193280
-0.0059691637962079400	2.20777786625326000	-58.569961360903500	1432.9533730704100
-0.0060067495391396800	2.22066403757604000	-57.422042418791900	1134.7975314575100
-0.0059271432288077500	2.20431811885098000	-54.558486904773400	806.2434692538370
-0.0065241428921705000	2.40034258703119000	-75.569591593897400	1380.9966963929900
-0.0071326453895658200	2.60016104367815000	-96.968994491525000	1967.7525557556200

-0.0068670717652983900	2.51180225459626000	-86.091482519233700	1293.4707170506800
-0.0066080996187082800	2.42621780678891000	-75.564863587558400	630.1635619486060
-0.0027499944993872900	1.27920173698376000	33.708602338064500	-2888.9896624906300
0.0012292098448456100	0.09953135610797750	145.382093906856000	-6465.5070089419600
-0.0011445896196868600	0.82476839680404300	73.206352785547100	-4337.7297450002700
-0.0035292262560758700	1.55390880913459000	0.557336028945568	-2193.5250822023900
-0.0007552725383181390	0.71408462324721100	80.207616494667700	-4818.8961823827700
0.0020343491305580100	-0.13010153578098800	160.228138281642000	-7455.0503277922600
-0.0000489128697604178	0.54035034157346000	88.318256560393900	-5163.3792093369500
-0.0021187215541491500	1.20792267960003000	16.460732901344900	-2867.8980129174000
-0.0002186450629023830	0.61096486511671600	75.296853092168200	-4937.2315578160000
0.0016897873425607500	0.01165861623529220	134.333989203916000	-7012.7043096668100
-0.0013703644620115600	0.97020225733657700	36.086791350250000	-3949.0496045306900
-0.0044247676629332900	1.92770991258900000	-62.197399963599500	-880.8679220298560
-0.0020110397644373000	2.62071408138583000	-180.033436096963000	2978.1495222870900
0.0003149936357854630	3.34349544060207000	-300.840835302062000	6929.1931225557200
0.0047303895884755400	3.21136573066259000	-328.978206510828000	7856.8023108690300
0.0091115721242572000	3.09153069094830000	-358.397018838086000	8825.0918131252200
0.0058431381036915500	1.64578779224155000	-135.088528564406000	1154.0363323432000
0.0026935964591158400	0.16016399513675100	92.144498680486900	-6637.8947709596400
0.0034916217260522100	-0.34186558060855600	146.411529314571000	-8400.8833603573200
0.0043099347001951400	-0.85019767794634600	201.245174350220000	-10180.0330987112000
0.0051256079450771800	-1.18450290063064000	240.477560970106000	-11773.1113095727000
0.0059438589528120300	-1.51963524895530000	279.790293458470000	-13368.9499230723000
0.0033202067243734400	0.23163339716652800	71.732369395715800	-6632.1655600206400
0.0006707119347221660	1.99193522583702000	-137.276822848916000	135.6127936139260
0.0052620613570425100	-0.17006147413119500	102.715160493906000	-7879.5436211463800
0.0098828830015582300	-2.34170957764146000	343.656036503314000	-15924.2763080722000
0.0049500531974266000	-1.13168848605187000	223.671643996963000	-11765.0083470851000
0.0000262157511035697	0.07546009994597720	103.932295631617000	-7611.9420305953600
0.0000977105153686703	0.07561545239256030	97.263233837302600	-7202.4783519119600
0.0001707235104987710	0.07536424406297330	90.623563950399400	-6793.6384966026700
-0.0018672049278971900	0.80431521496607300	6.738512272649200	-3810.9224926386200
-0.0039075112122042200	1.53413059963523000	-77.247237964520800	-824.5922188264910
-0.0054862566697231200	2.11072134804556000	-146.638298118066000	1736.4045670922700
-0.0070645803300132700	2.68730231086882000	-216.047778377839000	4298.5852824908400
-0.0106430719624780000	3.83368316205145000	-336.254586401780000	8304.3534506094300
-0.0142240639637712000	4.98089244979871000	-456.551168013609000	12313.1868958101000
-0.0170882112724071000	5.87687694989497000	-550.678644254713000	15500.8555343345000
-0.0193587012048870000	6.58869093998274000	-626.600233678726000	18124.3400682580000
-0.0192451134407474000	6.64862151899085000	-645.040376033629000	19105.8799026214000
-0.0191312429272974000	6.70854856157220000	-663.490671269828000	20088.0685956294000
-0.0186638100576415000	6.61089617811895000	-661.339325177947000	20264.7056207281000

-0.0181956661666339000	6.51307212840587000	-659.177719487677000	20441.2280431539000
-0.0194610520901267000	6.96621646775543000	-712.871825969062000	22432.3375867364000
-0.0207249473115384000	7.41893003114465000	-766.531041619603000	24422.6148241957000
-0.0193436604779907000	7.05935759368150000	-740.631813951230000	23908.5570990606000
-0.0179614512272821000	6.69955065288381000	-714.716112781119000	23394.1859915498000
-0.0183628666897039000	6.88473296221142000	-741.323446502475000	24507.4478734091000
-0.0176340898109916000	6.70253124937878000	-729.435722936122000	24334.7185475714000
-0.0139385093822263000	5.61403014834372000	-628.977452684914000	21374.4728506068000
-0.0102393167505672000	4.52441528039918000	-528.411956685734000	18410.9380312570000
-0.0104578568080051000	4.59274700445189000	-537.700410597676000	18815.0300970649000
-0.0106761849281673000	4.66102128766128000	-546.985005592183000	19219.0668471889000
-0.0106256666473066000	4.64386076279191000	-547.753318442306000	19351.6883467002000
-0.0105748764700811000	4.62662325315335000	-548.515832029351000	19484.1934428752000
-0.0075142427775650000	3.75737010727864000	-471.503764863384000	17314.5758775138000
-0.0044517596610379100	2.88757429897138000	-394.441865972929000	15143.4983883613000
-0.0055680864559581500	3.18582038827971000	-421.782748673022000	15984.8119523310000
-0.0061862827377842700	3.30756782863174000	-429.074569996611000	16108.7052050361000
-0.0050152754352855000	2.90331630435036000	-386.213437789698000	14680.3699025224000
-0.0038435008326140100	2.49881487537904000	-343.326715413401000	13251.2007299731000
-0.0015143991379726500	1.74836878424196000	-266.602292307445000	10744.3602897162000
0.0008157800910333330	0.99757952964776600	-189.843075191580000	8236.3899623776500
0.0021394877202944900	0.53166809742309600	-139.389682208226000	6521.0381007985300
0.0034641148179082800	0.06543503125493480	-88.901623587744700	4804.5120432430200
0.0046337546386180800	-0.33832125468089600	-45.860171623107400	3359.9117515294800
0.0058039814769664200	-0.74227006043630700	-2.798845802645400	1914.6586864468500
0.0072962800852165900	-1.24799624212421000	50.554924243342800	135.1598074731430
0.0087892734256962400	-1.75394894509846000	103.932003221431000	-1645.1033028535200
0.0102365129341140000	-2.20722102364616000	149.164258889143000	-3092.8471238030300
0.0116843245919986000	-2.66067112946789000	194.414201294638000	-4541.1552812219600
0.0127847457531754000	-3.05863436793592000	238.134116889286000	-6039.9999439519200
0.0138856564181287000	-3.45676206535083000	281.871312969858000	-7539.4199431304700
0.0152735429801531000	-3.90970429511631000	328.403638916420000	-9061.0448566051100
0.0166619437659180000	-4.36281046905540000	374.952548972381000	-10583.2062831190000
0.0180711376302653000	-4.83191678556931000	423.878299017709000	-12202.2370830891000
0.0194808563206815000	-5.30119274734644000	472.821401730391000	-13821.8343917535000
0.0189208433594269000	-5.18985951095816000	466.288810552637000	-13721.3972249526000
0.0174695159606486000	-4.80678177106021000	433.174068510144000	-12782.9823341245000
0.0167588359826184000	-4.62398304104452000	417.803962255607000	-12359.8306532818000
0.0160480618149421000	-4.44116247072294000	402.432240606171000	-11936.6410302103000
0.0168015775097724000	-4.68995383548124000	428.440943666584000	-12803.1046378012000
0.0175552792045236000	-4.93880613998335000	454.455983293143000	-13669.7785338384000
0.0163841537738320000	-4.63743295929410000	429.102903651796000	-12971.4037318087000
0.0152128729579772000	-4.33602370218116000	403.747150895607000	-12272.9659839896000

0.0157837425474156000	-4.54233605774121000	426.600815536064000	-13064.8834558037000
0.0163547810101800000	-4.74870683825043000	449.460780319909000	-13857.0153860072000
0.0151776008975459000	-4.42318654728482000	419.985899122095000	-12983.3534535009000
0.0133798446730849000	-3.89926901901334000	370.239416168082000	-11445.5014146334000
0.0119753569767282000	-3.48996117607509000	331.375235198896000	-10244.0625109499000
0.0105706444248832000	-3.08058780382311000	292.504832157127000	-9042.4312594573400
0.0089970129968663400	-2.62198664480106000	248.960202499004000	-7696.3019750337800
0.0074231296621146600	-2.16331207295914000	205.408602221660000	-6349.9572023918900
0.0061301960437737800	-1.78651427561408000	169.631281954142000	-5243.9448443025600
0.0048370554608508900	-1.40965616287655000	133.848234680975000	-4137.7554427965100
0.0032062118991214100	-0.93438175345824400	88.720463551403300	-2742.6852645627600
0.0015750948845816500	-0.45902765207808400	43.585125591924100	-1347.3811669821500

Appendix B

MCNP Codes for MTF Simulation

```
c the primary photons of 120 kVp spectrum after a water phantom,  100 μm
CdTe detector at 140 cm, collect flood field for LSF calculation
c Cell cards
c Detector cells
     3     10    -5.86    104   -105 106 -107 101 -103 fill=1 imp:p,e 1 $CdTe
     4     10    -5.86    202   -201 106 -107 101 -103 lat=1 u=1 imp:p,e 1
$lattice cell CdTe
c Air everywhere around detector
   303     3    -0.001293 (108 -999 -5 ) #3 imp:p,e 1
c    O  uter space
   999     0   999 :      5  :108 imp:p,e 0

c Surface cards
     5      pz      145 $End-of-the-problem plane
     101       pz 140 $End of air gap, top of metal plate
c   D etector planes
     103    pz    140.01   $End  of detector layer
     104    px   -5
     105    px  5
     106    py   -5
```

```
     107     py  5
     108     pz      138 $E nd-of-the-problem plane
c LSF in x direction - Lattice cell definition
     201     px 0.0005       $ 10 microns  bins
     202     px    -0.0005
c Air cylinder around the whole accelerator
     999      c    z  15


mode   p e
c Materials cards
m3     701   4.                -0.755636    $air (US S. Atm at sea level)
          8016.                -0.231475  18000.              -0.012889
m10    480  00.  0.5       52000.  0.5   $C         dTe
c source cards - 2-photons, source file at the bottom of water phantom
sdef X=d1 Y=d2 Z=139.9 dir=1 vec=0 0 1 erg=d3 par=2
si1    -0.00001 0.00001    $ 2 microns source size
sp1    0  1
si2    -6 6
sp2    0  1
c Primary only Spectrum from simulator + phantom +air at 171cm
# si3 sp3    $step ~0.02 MeV
0.02 0
0.020984 0.0010234
0.021967 0.0012398
0.022951 0.0015016
```

0.023934 0.0017982

0.024918 0.0020278

0.025902 0.0023026

0.026885 0.0024802

0.027869 0.0027364

0.028852 0.0029308

0.029836 0.0031356

0.03082 0.0031976

0.031803 0.0033368

0.032787 0.0034162

0.03377 0.0035754

0.034754 0.0036214

0.035738 0.0036028

0.036721 0.0036522

0.037705 0.0036658

0.038689 0.0036528

0.039672 0.0036666

0.040656 0.0035916

0.041639 0.0035678

0.042623 0.0035998

0.043607 0.0034788

0.04459 0.0034724

0.045574 0.0034116

0.046557 0.0033782

0.047541 0.0033326

0.048525 0.0032464

0.049508 0.0031674

0.050492 0.0031124

0.051475 0.003071

0.052459 0.0029634

0.053443 0.0029038

0.054426 0.002832

0.05541 0.0027988

0.056393 0.0031622

0.057377 0.0039814

0.058361 0.0048616

0.059344 0.00568

0.060328 0.005566

0.061311 0.0038862

0.062295 0.0026236

0.063279 0.0023552

0.064262 0.0021238

0.065246 0.0020946

0.06623 0.0021516

0.067213 0.0027764

0.068197 0.0030798

0.06918 0.0025288

0.070164 0.001984

0.071148 0.0016648

0.072131 0.0014094

0.073115 0.0013528

0.074098 0.0013034

0.075082 0.0012762

0.076066 0.0012274

0.077049 0.001189

0.078033 0.0011408

0.079016 0.001132

0.08 0.0010816

0.080984 0.0010782

0.081967 0.0010392

0.082951 0.0009976

0.083934 0.0009698

0.084918 0.0009106

0.085902 0.0008604

0.086885 0.0008492

0.087869 0.0008188

0.088852 0.0007906

0.089836 0.000729

0.09082 0.0007416

0.091803 0.0006704

0.092787 0.0006304

0.09377 0.0005992

0.094754 0.0005556

0.095738 0.000538

0.096721 0.00051

0.097705 0.000489

0.098689 0.0004504

0.099672 0.0004088

0.10066 0.0003894

0.10164 0.0003848

0.10262 0.000352

0.10361 0.0003442

0.10459 0.0003218

0.10557 0.0003026

0.10656 0.0002686

0.10754 0.0002588

0.10852 0.0002438

0.10951 0.0002224

0.11049 0.0002138

0.11148 0.0001948

0.11246 0.0001772

0.11344 0.0001582

0.11443 0.0001486

0.11541 0.0001302

0.11639 0.000115

0.11738 0.0000998

0.11836 0.000083

0.11934 0.0000656

0.12033 0.0000416

c D ose deposition tallies - in CdTe

```
c Tally for LSF
*F8:p (4<4[-512:512 0:0 0:0])
c
cut:e j 0.02        $time jumped, energy 10 keV (default and l. limit 1 keV)
cut:p j 0.01       $energy 10 keV from Varian sim paper(default is 1 keV)
PHYS:p 10 0 1 0 1 $Smpl phys>10MeV, brems, no coh, no photonuc, no Dopp
nps 10000000 $
```

Appendix C

MCNP Codes for NPS Simulation

```
c spectrum of simulator photons of energy 80kVp, 100 μm CdTe detector at 140
cm, collect flood field for NPS calculation.
c Cell cards
c Detector cells
      3     10    -5.86    104   -105 106 -107 102 -103 fill=1 imp:p,e 1 $CdTe
      4     10    -5.86    202   -201 204 -203 102 -103 lat=1 u=1 imp:p,e 1
$lattice cell CdTe
c Air everywhere around detector
   303     3    -0.001293 (108 -999 -5 ) #3 imp:p,e 1 $#2    #4
c    O   uter space
   999     0   999 :       5  :-108 imp:p,e 0

c Surface cards
     5      pz      142 $End-of-the-problem plane
c   D etector planes
     102    pz    140.3   $End  ofmetal  plate
     103    pz    140.31    $End of detector layer
     104    px    -10
     105    px  10
     106    py    -15
```

```
     107     py  15
     108     pz      138 $E nd-of-the-problem plane
c Lattice cell definition
     201       px 0.001 $ 0.002 cm bins (fmax=25 mm^-1)
     202     px    -0.001
     203     py 1.5       $ 3cm slit width
     204     py    -1.5
c Air cylinder around the whole accelerator
     999      c    z  37


mode   p e
c Materials cards
m3     701   4.               -0.755636    $air (US S. Atm at sea level)
          8016.               -0.231475 18000.              -0.012889
m10    480  00.  0.5       52000.  0.5   $C         dTe
c source cards - 2-photons, source file at the bottom of water phantom
sdef X=d1 Y=d2 Z=139.9 erg=d3 par=2 dir=1 vec=0 0 1
si1    -15 15
sp1    0  1
si2    -20 20
sp2    0  1
c Primary only Spectrum from simulator + phantom +air at 140cm
# si3 sp3    $step ~0.02 MeV
0.02 0
0.020984 0.0019644
```

0.021967 0.0023794

0.022951 0.0028012

0.023934 0.003186

0.024918 0.0036006

0.025902 0.003948

0.026885 0.0041782

0.027869 0.0045138

0.028852 0.0047328

0.029836 0.004903

0.03082 0.0049534

0.031803 0.0050894

0.032787 0.005116

0.03377 0.0051278

0.034754 0.0051218

0.035738 0.0051032

0.036721 0.0050852

0.037705 0.0050096

0.038689 0.0049494

0.039672 0.0048172

0.040656 0.0047934

0.041639 0.0046614

0.042623 0.0045138

0.043607 0.0044126

0.04459 0.0042884

0.045574 0.0041646

0.046557 0.0041142

0.047541 0.0039472

0.048525 0.0038188

0.049508 0.0036726

0.050492 0.003544

0.051475 0.0034186

0.052459 0.0032374

0.053443 0.0031038

0.054426 0.0030288

0.05541 0.002828

0.056393 0.0027858

0.057377 0.0028184

0.058361 0.0028918

0.059344 0.0029904

0.060328 0.0028116

0.061311 0.002358

0.062295 0.002013

0.063279 0.0018742

0.064262 0.0017218

0.065246 0.0015888

0.06623 0.0015252

0.067213 0.0015178

0.068197 0.0014126

0.06918 0.0012308

0.070164 0.0010436

0.071148 0.0009042

0.072131 0.0007736

0.073115 0.0007248

0.074098 0.0006694

0.075082 0.0005778

0.076066 0.0005228

0.077049 0.0004658

0.078033 0.0003802

0.079016 0.0003214

0.08 0.0002498

cDose deposition tallies - in CdTe

c Tally for flood field Dose deposition

*F138:p (4<4[-2047:-1536 -3:3 0:0])

*F128:p (4<4[-1535:-1024 -3:3 0:0])

*F118:p (4<4[-1023:-512 -3:3 0:0])

*F8:p (4<4[-511:0 -3:3 0:0])

*F18:p (4<4[1:512 -3:3 0:0])

*F28:p (4<4[513:1024 -3:3 0:0])

*F38:p (4<4[1025:1536 -3:3 0:0])

*F48:p (4<4[1537:2048 -3:3 0:0])

cut:e j 0.03 $time jumped, energy 10 keV (default and l. limit 1 keV)

cut:p j 0.01 $energy 10 keV from Varian sim paper(default is 1 keV)

PHYS:p 10 0 1 0 1 $Smpl phys>10MeV, brems, no coh, no photonuc, no Dopp

RAND SEED=9878762211153

nps 100000000 $